

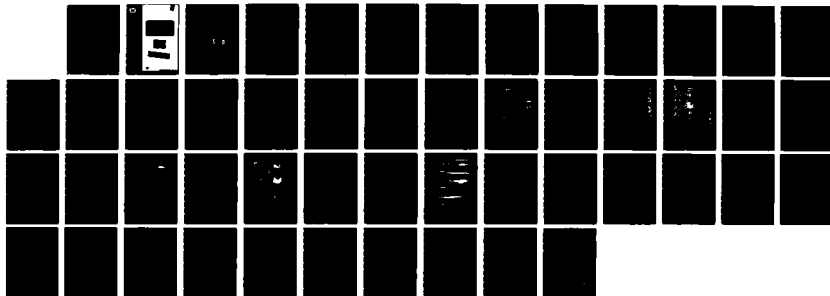
NO-A102 889

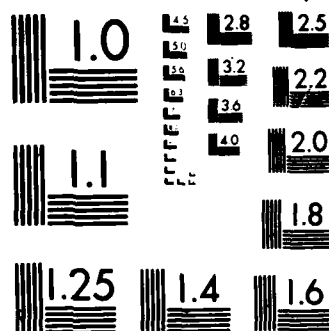
SEA ICE SIMULATIONS PERFORMED WITH FORCING FIELDS
SPECIFIED FROM A GENERA (U) MAX-PLANCK-INST FUER
METEOROLOGIE HAMBURG (GERMANY F R) P LOEW 26 JUN 87
R/D-5451-EN-01 DAJ455-86-M-0293 F/G 8/12

1/1

UNCLASSIFIED

NL





MICROCOPY RESOLUTION TEST CHART
NATIONAL BUREAU OF STANDARDS 1963-A

ORIGINAL FILE COPY



US Army Corps
of Engineers

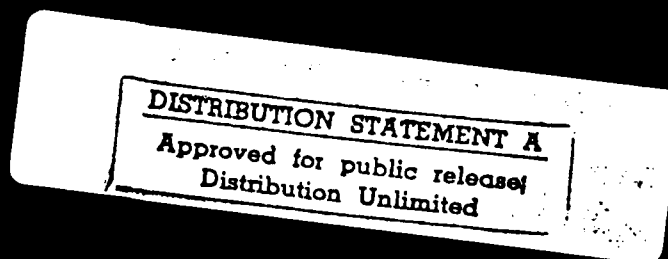
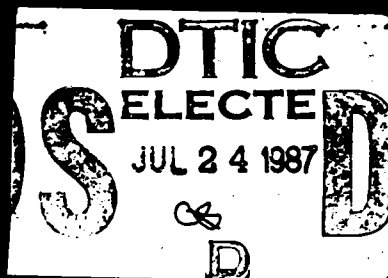
AD-A182 889

6

FINAL TECHNICAL REPORT 6/87

SEA ICE SIMULATIONS

PERFORMED WITH FORCING FIELDS
SPECIFIED FROM A GENERAL CIRCULATION MODEL
AS A STEP TOWARD
MODELING THE CLIMATE SYSTEM IN TOTAL



Cold Regions Research and
Engineering Laboratory

72 Lyme Road • Hanover • New Hampshire 03755

87 7 21 156

6

FINAL TECHNICAL REPORT 6/87
SEA ICE SIMULATIONS
PERFORMED WITH FORCING FIELDS
SPECIFIED FROM A GENERAL CIRCULATION MODEL
AS A STEP TOWARD
MODELING THE CLIMATE SYSTEM IN TOTAL

DTIC
ELECTE
JUL 24 1987
S D D

DISTRIBUTION STATEMENT A
Approved for public release
Distribution Unlimited

Unclassified

SECURITY CLASSIFICATION OF THIS PAGE

REPORT DOCUMENTATION PAGE

Form Approved
OMB No 0704-0188
Exp. Date Jun 30, 1986

1a. REPORT SECURITY CLASSIFICATION Unclassified			1b. RESTRICTIVE MARKINGS		
2a. SECURITY CLASSIFICATION AUTHORITY			3. DISTRIBUTION/AVAILABILITY OF REPORT Approved for public release; distribution unlimited.		
2b. DECLASSIFICATION/DOWNGRADING SCHEDULE			5. MONITORING ORGANIZATION REPORT NUMBER(S) R&D 5451-EN-01		
4. PERFORMING ORGANIZATION REPORT NUMBER(S)			7a. NAME OF MONITORING ORGANIZATION USARDSG-UK		
6a. NAME OF PERFORMING ORGANIZATION Max Planck Institut fuer Meteorologie		6b. OFFICE SYMBOL (If applicable)		7b. ADDRESS (City, State, and ZIP Code) Box 65 FPO NY 09510-1500	
6c. ADDRESS (City, State, and ZIP Code) Bundesstr. 55 2000 Hamburg 13, F.G.R.		8a. NAME OF FUNDING/SPONSORING ORGANIZATION Cold Regions Research & Engineering Lab.		8b. OFFICE SYMBOL (If applicable) CRREL	
8c. ADDRESS (City, State, and ZIP Code) 72 Lyme Road Hanover, NH 03755		9. PROCUREMENT INSTRUMENT IDENTIFICATION NUMBER DAJA45-86-M-0293			
10. SOURCE OF FUNDING NUMBERS					
PROGRAM ELEMENT NO. 61102A		PROJECT NO. L161102BH57		TASK NO. 01	
WORK UNIT ACCESSION NO.					
11. TITLE (Include Security Classification) (U) Sea Ice Simulations Performed With Forcing Fields Specified From a General Circulation Model and with a Fully Coupled Air-Ice Model as a Step Toward Modeling the Climate System in Total					
12. PERSONAL AUTHOR(S) Loewe, Peter					
13a. TYPE OF REPORT Final		13b. TIME COVERED FROM 3/86 TO 3/87		14. DATE OF REPORT (Year, Month, Day) 1987-06-26	
15. PAGE COUNT 12 p., 29 figs.					
16. SUPPLEMENTARY NOTATION Coupled simulations are not reported in this document					
17. COSATI CODES			18. SUBJECT TERMS (Continue on reverse if necessary and identify by block number)		
FIELD	GROUP	SUB-GROUP	Air-Ice-Interaction - Arctic Sea Ice - Atmospheric circulation		
08	12		Climate Modeling - Coupled Models - Ice Dynamics		
			Ice Thermodynamics		
19. ABSTRACT (Continue on reverse if necessary and identify by block number)					
<p>As a first step in the development of a fully coupled atmospheric/ice model including ice dynamics, an Interannual simulation of the Arctic ice cover with GCM simulated surface fluxes and winds is compared to a Control equilibrium simulation using observed atmospheric forcing. In both cases a full dynamic-thermodynamic sea ice model (Hibler, 1979) employing a viscous plastic ice interaction is utilized. For the simulated forcing results from a coarse resolution GCM (Roachner, 1979) with specified sea surface temperatures and ice extents, but simulated cloud cover, are used. For the observed data, climatological temperatures and winds (with daily fluctuations added) are employed. Results from a thermodynamic sea ice model subjected to the simulated forcing are also reported for comparison. Main fields as ice thickness, compactness, and drift as well as radiative and wind forcing are analyzed, both in terms of the seasonal cycle and in terms of interannual variability. An analysis of regional mass budget and longitudinal variability of key variables is presented in addition to results covering the full spatial domain. Amplitude and phase of simulated annual cycles of total ice mass and extent (Fig. A0) are in good agreement with those of the Control cycles; the annual mean thickness being 2.5m and ice extent in summer being 50% of the extent in winter. The simulated spatial distribution of ice is however considerably distorted. Large portions of the Arctic Ocean become ice free each summer while marginal seas stay ice covered. This is caused by a wind forcing that,</p>					
20. DISTRIBUTION/AVAILABILITY OF ABSTRACT <input checked="" type="checkbox"/> UNCLASSIFIED/UNLIMITED <input type="checkbox"/> SAME AS RPT. <input type="checkbox"/> DTIC USERS			21. ABSTRACT SECURITY CLASSIFICATION Unclassified		
22a. NAME OF RESPONSIBLE INDIVIDUAL Jerry C. Comati			22b. TELEPHONE (Include Area Code) 01-402-7331		22c. OFFICE SYMBOL AMXSN-RE

DD FORM 1473, 84 MAR

83 APR edition may be used until exhausted.
All other editions are obsolete.

SECURITY CLASSIFICATION OF THIS PAGE

Unclassified

about

19. Abstract (cont'd)

is generally simulated too stationary and too strong on account of the GCM's low resolution. Vigorous winds cause also the build up of heavy ice i.e. in the Bering Strait and Greenland Sea area, where thermal forcing suggests rather thin or no ice. Such out of place thick ice might affect the atmospheric circulation in the coupled model via associated very low surface temperatures. It is clear that such interaction is not possible in a coupled model employing only static sea ice. (The impact of an ice free Arctic Ocean is beyond question). The coupled model is likely to produce even less realistic results than those presented here. Nevertheless, we trust that a fully coupled simulation, to be carried out in the immediate future with this model, is appropriate to increase the understanding of the coupled air-ice system. In the long run, however, a better resolving atmospheric model must be employed.



Accession For	
NTIS CRA&I	<input checked="" type="checkbox"/>
DTIC TAB	<input type="checkbox"/>
Unannounced	<input type="checkbox"/>
Justification	
By	
Distribution /	
Availability Codes	
Dist	Avail and/or Special
A-1	

CONTENTS

Report Documentation Page / Abstract

1 Introduction	1
2 Uncoupled Experiments	1
3 Resolution Related Problems	2
a) Incommensurate Turbulent Heat Fluxes	2
b) Zonally Asymmetric Forcing Fields	3
4 Analysis of Experiments	4
a) Geographical Distribution of Ice Thickness and Drift	4
b) Interannual Variability of Ice Thickness and Compactness	6
c) Estimated Melt Potential of Net Radiative Fluxes	7
d) The Wind Driven Deterioration of the Arctic Ice Cover	9
5 Outlook	10
Acknowledgements	11
References	12

FIGURE CAPTIONS

- [1] Grid Configuration as utilized for forced sea ice simulations.
- [2] Time-longitude section along 78.75°n.lat. for observed and modeled incoming Long-wave Radiation.
- [3] Time-longitude section along 78.75°n.lat. for observed and modeled incoming Solar Radiation.
- [4] Time-longitude section along 78.75°n.lat. for Ice Thickness patterns as produced with a Semtner-type thermodynamic sea ice model.
- [5] Time-longitude section along 78.75°n.lat., showing Ice Thickness patterns for the 4th and 5th year of the Control Experiment and for the Interannual Forcing Experiment as produced with the full dynamic thermodynamic sea ice model.
- [6] Geographical distribution of Ice Thickness for every other month of the 5th year of the Control Experiment.
- [7] Seasonal and annual mean Ice Drift vectors for the 5th year of the Control Experiment together with annual mean Ocean Currents.
- [8] Geographical distribution of the 6-year mean Ice Thickness for every other month of the Interannual Experiment.
- [9] Geographical distribution of Ice Thickness for every other month as produced with a Semtner-type thermodynamic sea ice model.

- [10] 6-year mean seasonal and annual mean Ice Drift vectors for the Interannual Experiment.
- [11] Geographical distribution of Ice Thickness Differences (Interannual minus Control) for every other month.
- [12] Ice Velocity vectors for January, February, and March of Year 8 and of Year 9 of the Interannual Experiment.
- [13] Surface Radiative Fluxes, June-July-August means.
- [14] Divergence and Persistence of the ice velocity field during March-April-May and ice compactness in May.
- [15] Time-longitude section along 78.75°N .lat. for modeled Sea Level Pressure.
- [16] Observed Geostrophic Winds, June-July-August mean.
- [17] Modeled Geostrophic Winds, June-July-August mean of GCM-data Year 9.
- [18] Divergence and Persistence of the ice velocity field during June-July-August and ice compactness in August.
- [19] Northern Grid Configuration to be utilized for global coupled air-ice simulations.
- [20] Southern Grid Configuration to be utilized for global coupled air-ice simulations.

TABLES

Table I: Melt potential of simulated and observed net radiative fluxes.

APPENDIX A: Graphical Documentation of Mass Budget*

- [A0] Annual cycles of monthly and over the entire grid domain averaged Ice Thickness (or Total Mass) and Ice Compactness (or Total Extent) for the Control and the Interannual simulation.
- [A1] As in A0 except for Region I (Bering Strait).
- [A2] As in A0 except for Region II (Canadian Arctic).
- [A3] As in A0 except for Region III (Central Arctic).
- [A4] As in A0 except for Region IV (East Greenland Sea).
- [A5] As in A0 except for Region V (Laptev Sea).
- [A6] As in A0 except for Region VI (Norwegian Sea).
- [A7] As in A0 except for Region VII (Barents Sea).
- [A8] As in A0 except for Region VIII (Kara Sea).

* a discussion is provided in section 4b

FINAL TECHNICAL REPORT 6/87

SEA ICE SIMULATIONS PERFORMED WITH FORCING FIELDS SPECIFIED FROM A GENERAL CIRCULATION MODEL AS A STEP TOWARD MODELING THE CLIMATE SYSTEM IN TOTAL

by

Peter Loewe

Max-Planck-Institut fuer Meteorologie
Bundesstr.55, 2000 Hamburg 13, F.R.G.

1 Introduction

The main goal of this research is to develop and numerically investigate a fully coupled atmosphere-ice model. The main unique feature of this modeling effort is the inclusion of full ice dynamics. In particular, while a number of previous investigators have examined Atmospheric circulation models together with thermodynamic sea ice in an oceanic mixed layer [e.g. Manabe and Stouffer (1980), Pollard et.al. (1983)], to date no full simulation including full ice dynamics has been performed.

To carry out such a study, the dynamic thermodynamic sea ice model developed by Hibler (1979/80) is being coupled to an atmospheric circulation model [Roeckner, 1979] including a motionless oceanic mixed layer with variable depth [Biercamp, 1986].

2 Uncoupled Experiments

Because of the large number of degrees of freedom of such a coupled model, the probability of drifting away from reality is quite high. Therefore as a *Control Experiment*, a sea ice simulation utilizing observed atmospheric forcing prepared by Hibler (1986, private communication) for use in a coupled ice ocean model, was carried out. This forcing consisted of climatological atmospheric temperatures and humidities together with daily varying wind fields. Temperatures and humidities served as input for simple bulk aerodynamic formulas providing the surface sensible and latent heat fluxes. The wind fields were obtained by

merging monthly mean wind fields averaged over a 30 year period (Walsh et. al., 1985) with daily deviations from the monthly mean geostrophic wind fields from the FGGE year (1979). The incoming solar and longwave radiation fields were computed from the Zillman and the Jackson and Idso formula respectively, as described i.e. in Parkinson and Washington (1979). Annual mean ocean currents were taken from a coupled ice-ocean simulation carried out by Hibler and Bryan (1987). These currents were also used in experiments employing modeled atmospheric forcing. Simulations of this type have been used by Hibler (1979/80) in evaluating the performance of the dynamic thermodynamic sea ice model, and have been shown to reproduce many of the observed features of ice build up, decay and drift.

The observed forcing fields cover a period of one year but were applied to the dynamic thermodynamic sea ice model repeatedly in order to reach a cyclic equilibrium after five years. The fifth annual cycle of this Control Experiment is taken as the reference cycle with which simulations utilizing modeled atmospheric forcing fields can be compared.

For comparison to this Control Experiment, and as an initial step toward a fully coupled simulation, an *Interannual Experiment* employing six consecutive years of GCM-generated forcing fields was carried out. The GCM forcing fields for this experiment were obtained from a global GCM simulation with prescribed sea ice limits and SST [Alexander and Mobley, 1976] conducted by Roeckner (1985, private communication). This Interannual Experiment was designed to reveal whether or not characteristic features obtained from earlier *equiannual experiments* with cyclic modeled forcing were typical in the sense that they would reappear every year or remain unchanged. Another issue was to examine if the ice showed any persistent trend that might eventually lead to extreme states.

Before commenting on results obtained from both simulations we shall discuss some problems regarding the modeled forcing. In particular the paragraph on the zonal asymmetry of the forcing greatly aids understanding the tremendous differences in simulated features of the Arctic ice cover.

3 Resolution Related Problems

The atmospheric model operates on a spherical grid with a meshwidth of 11.25° . As a consequence, the Arctic Basin is resolved by no more than 25 grid points along the 78.75° parallel - 250km apart from one another and 1250km south of the grid point at the pole. The sea ice model, on the other hand, is defined on an area conserving Lambert equivalent square grid with $\Delta x = \Delta y = 160\text{km}$. Fig. 1 illustrates the grid utilized for the forced sea ice simulations.

a) Incommensurate Turbulent Heat Fluxes

In order to drive the ice model with GCM-generated forcing fields these fields had to be interpolated to the ice grid. This was readily done for downward radiative fluxes and surface pressure. The sensible and latent heat fluxes, however, required a more sensitive treatment. This will be evident from what follows.

Surface heat fluxes strongly depend on surface characteristics and particularly on the surface temperature. Accordingly they mirror the type of surface they are computed for.

A pronounced temperature contrast between air and ocean in winter and air and land in summer means an energy loss for the respective surface type on the order of several hundred W/m^2 . However, heat fluxes over an ice surface typically lie in a relatively narrow range of $\pm 10 W/m^2$. Applying fluxes computed for a GCM's ocean or land grid point to an ice surface carelessly can cause a missing melt season in the land/summer case and inadmissible ice surface temperatures below $0^\circ K$ in the ocean/winter case. A linear interpolation scheme would still provide too low values at positions between a GCM's ice grid point and a GCM's ocean or land grid point. Since it is the ice edge that abruptly separates the different flux regimes, the position of the ice edge could serve as an ideal weighting parameter, if it was not desired to be part of the ice model's output.

A simple method to overcome this problem is the following. Before entering the interpolation scheme the fluxes are set to zero if the GCM's surface temperature is above freezing and if at the same time the fluxes are pointing towards the atmosphere. This condition eliminates cases of the above mentioned kind. On the other hand, fluxes pointing toward the surface with a higher than freezing temperature are left unchanged. The idea here is that if the actual surface was replaced with a necessarily cooler ice surface the latter was likely to gain even more energy than the flux supplied the original warmer surface with.

It must be admitted that the described procedure is somewhat arbitrary, but so is the interpolation scheme itself. Fortunately, we shall not have to deal with the heatflux problem in the fully coupled model, for the modified GCM is capable to handle hybrid grid cells composed of ice, ocean, and land as well. The fluxes are determined for each individual surface type in order to do the heat budgets separately. The resulting different surface temperatures will be averaged using some kind of weighting procedure.

b) Zonally Asymmetric Forcing Fields

The most serious consequence of the GCM's coarse resolution is its overestimation of stationary waves. The means of communication between continental and oceanic regimes - transient eddies - are poorly resolved by the grid. The pressure pattern is therefore largely determined by the geographical distribution of land and sea and their different thermal properties and states. The asymmetry of the lower boundary not only affects the pressure field but also cloud cover, precipitation, and most relevant to us the surface energy fluxes. This is verified easily from Fig. 2 and Fig. 3 showing the incoming shortwave and longwave radiation along a section of the 78.75° parallel for the six consecutive years of the GCM-forcing data set. For comparison the fluxes used for the Control Experiment are also shown. Extreme low rates of atmospheric radiation ($< 150 W/m^2$) are indicative of the low heat budget of the polar atmosphere in continental regimes during winter. This is again because overtaxed stationary eddies have to bring about the meridional transports almost all alone. In summer the longwave fluxes are still small here on account of prevalent clear skies which allow short wave fluxes in excess of $300 W/m^2$.

Results from an experiment originally designed to test the applicability of the flux fields after interpolation and clearing demonstrate how this asymmetry of the forcing translates to static sea ice. For this test a diagnostic Semtner-type sea ice model including parameterizations for leads, internal melt, and albedo was equiannually driven for a period of ten years with Year 6 of the GCM-forcing data set; (Year 6 is actually the first year of the available data set and refers to the sixth year of the multiannual GCM-simulation

the data were taken from). Fig. 4 shows the ice thickness performing equilibrium cycles after the second year at most of the gridpoints along 78.75° . Two sections of heavy ice fall into continental regimes where surface temperatures as low as -50°C are associated with strong growth rates in winter. Two intermediate sections of relatively thin ice are governed by the oceanic regimes characterized by moderate radiative fluxes of either kind. The asymmetric pattern of the forcing is essentially copied to the ice thickness field. As will be shown soon the response of a sea ice model employing full dynamics turns out to be quite different.

In order to prevent excessive ice growth in a coupled model experiment employing this thermodynamic sea ice model Roeckner (1986, private communication) introduced a locally constant artificial flux to the heat budget. This corrective flux was determined from the same GCM simulation that produced our raw data set as the 10-year mean net heatflux through the surface. As a side effect such modification can zonalize the ice thickness and the surface temperature field, to name only two.

For the time being, we shall not apply this or any other flux correction method. We are not primarily interested in realistic results yet, but in the as much as possible unmanipulated response of the full ice model.

4 Analysis of Experiments

First of all it is useful to know that the Interannual Forcing Experiment has been initialized with the final state of the Control Experiment. To contrast these two experiments and illustrate the transition, Fig. 5 shows another time-longitude section for ice thickness as obtained from these two simulations. This figure can also be compared with Fig. 4 which shows results from a thermodynamics only model subjected to Year 6 of the Interannual forcing.

The overall shape of the Control thicknesses is obviously zonal. The Interannual thicknesses, on the other hand, do not show a zonal pattern, nor do they exhibit anything comparable to the aesthetic asymmetry of the thermodynamically obtained thickness patterns of Fig. 4. The thickness patterns of these three simulations virtually have nothing in common. It is only that this chaotic interannual pattern is similar to itself, indicating a relatively small interannual variability of the forcing fields.

a) Geographical Distribution of Ice Thickness and Drift

For a more complete impression thickness and velocity fields covering the entire grid domain are analyzed here for the Control and the Interannual simulation.

In Fig. 6 monthly means of ice thickness for every other month illustrate the equilibrium thickness cycle as of the Control simulation. The frames for September and March represent the minimum and maximum of this cycle. The retreat of ice during summer uncovering most of the marginal seas is simulated in favorable agreement with observations. The thickness stays in a reasonable range, nowhere ever exceeding 5m. The thickest ice is found in the Canadian Arctic which is in agreement with what scarce submarine data suggest. This major deviation from a zonally symmetric field is mainly caused by the convergent ice flow in that region as is evident from the annual mean velocity field given in Fig. 7.

In addition to this, the annual mean field also exhibits the classical features of the Arctic ice drift, namely the Beaufort Sea Gyre and the Transpolar Drift. It should be noted however, that these characteristics undergo a seasonal cycle. They are particularly well developed in the fall but less pronounced in spring and summer. It is furthermore evident from Fig. 7 that the classical pattern is significantly shaped by the annual ocean current forcing. This is especially true in summer, when a weak sea level pressure distribution is associated with apparently negligible wind forcing.

In Fig. 8 the 6-year average seasonal thickness cycle as obtained from the Interannual simulation is shown. After having taken cognizance of Fig. 5 it is not exactly surprising to see that the patterns of Fig. 8 and Fig. 6 are as different as day from night.

Virtually the only similarity between Figs. 6 and 8 is that again the frames for March and September represent the maximum and minimum ice extent. As is evident from the whole set of frames, however, there is almost no advance and retreat of the ice in the seas adjacent to the Central Arctic Basin. Results from the earlier mentioned forced thermodynamic simulation (see Fig. 9) as well as ice drift patterns (Fig. 10) indicate that this is attributable to ice export from the Basin during summer, as far as the East Greenland and the Norwegian Seas (Regions IV and VI) are concerned. This is also reflected by the balloony shape of the thickness pattern in the heavy ice region of the East Greenland Sea during this season. Actually, the thickest ice is found here.

In contrast, the situation in the Barents and Kara Sea (Regions VII and VIII) appears to be largely determined by thermodynamical processes. Excessive growth in the course of the winter due to a cold continental climate here prevents a complete melt down in summer.

Another zone of heavy ice around the Bering Strait (Region I) is created by shoreward directed winds associated with the northern fringe of the Aleutian Low. It is interesting to note that the growth cycle here is interrupted during December and January, when in some winters a more offshore oriented flow can establish. This appears to be related to a westward shift of the Aleutian Low. In this case a look beyond the ice domain is really required to understand the relation to the atmospheric circulation.

The most dramatic event to mention is that vast areas of the Central Arctic as well as the Canadian Arctic (Regions III and II) become ice free each summer. What causes this will be discussed in somewhat greater detail in subsequent sections.

How essential the deviations between thicknesses obtained from the Control and the Interannual Experiment are may become even clearer from Fig. 11 which shows 6-year mean minus Control thicknesses.

In Fig. 10 the 6-year mean seasonal and annual ice velocity fields are presented. A comparison with the Control fields of Fig. 7 reveals that the ice in the Interannual case generally drifts at about twice the Control speed. This is mainly caused by a surface pressure distribution that is simulated too stationary. Far too high pressure during the cold seasons is merely a consequence of this. Thus, the derived wind forcing tends to be too persistent and too strong. The main unique feature (resulting from the foregoing) is the pronounced cyclonical drift pattern in summer. It is only then and in the fall that we observe a noticeable outflow from the Arctic Basin. The classical drift pattern is visible in outlines in spring and in fall.

b) Interannual Variability of Ice Thickness and Compactness

Spatial compression of thickness and compactness data makes it feasible to focus on the evolution of these fields over the full temporal length of the Interannual simulation. Fig. 1 defines the geographic domain covered by the sea ice model and shows the regions this domain is subdivided in for averaging purposes. We do not intend to discuss here the conditions for each and every Region. A complete set of graphs showing regional time series for thickness and compactness is provided in Appendix A, however. We describe briefly here the results from this set of graphs.

In Fig. A0 monthly means of thickness and compactness fields averaged over the entire domain are displayed for the 5th year of the Control Experiment and for each individual year of the Interannual Experiment. It can be seen easily that the model is drifting away from the *observational equilibrium cycle* during the first year of the Interannual simulation. The subsequent cycles do not show any trend but fluctuate irregularly within a *quasi-equilibrium range* around the 6-year mean cycle - the new equilibrium cycle associated with the GCM-climate. The rather narrow range reflects that there is only little interannual variability in the atmospheric forcing. The variability of stationary atmospheric waves can obviously not make up for a lack of variability on shorter time scales associated with underestimated transient processes. It is perhaps also significant that the forcing is taken from a simulation with prescribed ice limits having no interannual variability.

On the whole, the ice in the Interannual Experiment tends to be more compact and thicker than in the Control Experiment. This is likely due to the combined effect of a cooler than observed GCM-simulated surface climate on the one hand, and due to more vigorous and shoreward directed wind fields on the other.

In spite of the difference between the 6-year mean cycle and the Control cycle, the data averaged over the entire domain, amazing enough, can be judged as fairly resembling one another. That this does not hold on a regional basis is clear. It is only mutual cancellation what allows the domain averages to compare so favourably.

While the thickness and compactness cycles in general differ only slightly from one year to the other, those of Region V (Fig. A5) and particularly of Region I (Fig. A1) exhibit a quite broad range of variability. Conditions of least ice mass and extent in Region I during Year 8 are immediately succeeded by highest values of these variables in Year 9 of the Interannual Experiment. From Fig. A5 it is evident that the reverse took place in Region V. Particularly remarkable is that the ice export rates equal or even exceed the local production rates during much of the 'growth' season of each Region's 'minimal' yearly cycle. The corresponding symbols of the respective graph run parallel to the time axis in this case.

An explanation for this episode and a proof for the communication between both regions is readily found by comparing the mean ice drift patterns for the first quarter of Year 8 and Year 9 on a monthly basis (Fig. 12). Where heavy ice conditions are going to evolve clearly depends on the relative positions and intensities of the Aleutian Low and the Beaufort High.

The heavy ice in the East Greenland Sea (Region IV) again shows hardly any interannual variability and is characterized by a flat yearly thickness cycle (Fig. A4). It is interesting to note that the ice in this area is essentially at rest from December through

May but moves at speeds of 10cm/s and higher during the warmer seasons. The pressure gradients are spuriously high here, especially in summer. This may be, at least in part, a consequence of the fact that the derived sea level pressure over the Greenland plateau is inherently fictitious. The departure of the first interannual cycle from the Control cycle takes place only when the Asian summer low begins to govern an ice circulation that is associated with high export rates into this area. By mid October the ice has arrived at an average thickness of about 5m due to ridging and varies only slightly around this value throughout the rest of the simulation. The ice mass in Region IV is therefore mainly determined by a balance between summer melt and ice import from Region II at the same time. During the motionless winter season, however, it finds itself in a state of thermodynamic equilibrium.

Fig. A2 and Fig. A3 show again that major parts of the Arctic Basin become ice free during summer. It is also evident that this is not an isolated event but a recurrent pattern. To what degree this systematical bias is to be attributed to the radiative forcing and to the wind forcing is examined in the sections to follow.

c) Estimated Melt Potential of Net Radiative Fluxes

A rough estimate of the role of net radiation in the nearly complete removal of the sea ice from the Arctic Basin may be obtained from this simple model.

The differential change in thickness dz due to the net radiative flux R_i over the ice covered portion of a grid cell can be written as

$$dz = -\frac{R_i}{L} dt \quad (1)$$

where L denotes the volumetric heat of fusion. The change in the open water fraction da due to the net radiative flux R_w over the open water may be written as

$$da = \frac{R_w a}{L z(t)} dt \quad (2)$$

provided R_w causes only lateral melt. Assuming that R_w and R_i are constant in time we arrive at

$$z(t) = z_0 - R_i t / L \quad (3)$$

and

$$a(t) = a_0 \left(1 - \frac{R_i t}{L z_0} \right)^{-R_w / R_i} \quad (4)$$

An evaluation of eq.(3) and eq.(4) leads to the results shown together with substituted input data in Table I.

Among the conclusions that can be drawn from the contained information are, for one: There is not too much of a difference between the amounts of net radiation gained over ice (R_i) in the Interannual and in the Control case. It is only in the less critical Region I

where eq.(3) predicts a change in thickness in excess of 1m for both simulations. Vertical melt therefore is of minor relevance, and, in addition, is in good agreement with the rates of the Control simulation. For two: The amounts of radiative energy gained over leads (R_w) in the Interannual case obviously are up to 50% higher than the Control data suggest. According to eq.(4), however, the way these leads grow is much more determined by the fraction of the net radiative fluxes R_w/R_i and by the fraction R_i/z_0 . These values, given in row 3 and 4 of the table, actually resemble one another fairly well (with the exception of R_w/R_i in Region II being 70% higher than in the Control case). In this context, it is also interesting to note that the flux fractions of Region I are virtually equal, whereas the individual fluxes show the highest deviations from one another.

Table I. Melt potential of simulated and observed net radiative fluxes.*

	Interannual Experiment			Control Experiment		
	Region I	Region II	Region III	Region I	Region II	Region III
$R_i(JJA)$	56.17	23.24	31.86	41.53	31.98	29.52
$R_w(JJA)$	207.00	168.97	175.36	145.21	135.88	133.28
R_w/R_i	3.69	7.27	5.50	3.50	4.25	4.52
R_i/z_0	13.87	6.79	9.34	13.91	7.78	9.79
$z_0(May)$	4.05	3.42	3.41	2.99	4.11	3.02
$z(Aug)$	3.10	1.74	1.62	1.78	3.47	2.58
$z(eq.3)$	2.60	2.82	2.59	1.91	3.28	2.25
$a_0(May)$	0.07	0.04	0.06	0.02	0.01	0.01
$a(Aug)$	0.59	0.69	0.68	0.54	0.15	0.23
$a(eq.4)$	0.35	0.14	0.30	0.10	0.02	0.06
a/a_0	5.11	4.06	4.56	4.73	2.59	3.72

* The comparison is based on the evaluation of equation (3) and (4). For the fluxes [W/m^2] regional averages of the 6-year mean JJA quarter or the 5th years JJA quarter were utilized in the Interannual case and the Control case respectively. (For the definition of Regions see Fig. 1). As initial values for thickness m and open water fraction [%] accordingly averaged monthly means of May were substituted. Corresponding values for August are also reported for comparison. Note, that all thickness values given here denote the thickness of the ice covered portion of a region rather than the mean thickness ($z \cdot (1 - a)$) of that region. t was set to 3 months in seconds.

If all these differences are minor what causes the tremendous differences in the amount of open water as derived from eq.(4)? The answer is: small differences in the initial amount of open water ($a_0(May)$). This can be verified from the last row of the table.

What we conclude from all this now is that if one had turned off dynamical processes during May of the Interannual simulation the gain of radiative energy during JJA had reached out to melt about half of the actually simulated amount of melted ice within Region I and Region III. Most of the ice contained in Region II would still reside there, however. The other interesting point here is that the net radiative fluxes of the Control Experiment evidently led to similar results if (in addition to switched off dynamics) the open water fractions in May were of the same size as in the Interannual simulation.

This suggests that the recurrent pattern of an ice free Arctic during the Interannual Experiment is not primarily related to an erroneous radiative forcing. This is a relieving finding, in particular on account of the strong deviations of both, the incoming solar and longwave radiative fluxes from the Control fluxes (Fig. 13). Fortunately, these errors - obviously related to an underestimated cloudiness and the problem to resolve Arctic stratus in a GCM - mostly cancel as far as the way radiation is related to melt rates is concerned.

The extensive decay of Central Arctic ice is induced by the wind and completed in collaboration with the radiative forcing. This will be shown next.

d) The Wind Driven Deterioration of the Arctic Ice Cover

The Arctic ice cover is already in May relatively unconsolidated in the Interannual case. Sizable amounts of open water are visible in the coastal regions of the New Siberian Islands and the Canadian Arctic (Fig. 14). This is clearly related to an offshore directed divergent ice drift in spring (Figs. 10, 14). As was shown in the previous section, however, the subsequent rigorous deterioration of the pack should have not occurred if dynamical processes had been inactivated in June, July, and August. It is therefore only consequent to investigate the dynamical features of the ice drift and the governing wind forcing during this season.

Fig. 15 illustrates the temporal evolution of GCM simulated sea level pressure along 78.75° . The pressure is simulated some 30hPa higher than observed during the cold seasons (primarily on account of the GCM's low resolution). To our delight the pressure range in summer is in much better agreement with observations. Actually, it is then when the agreement is closest. A serious withdraw, however, is the low interannual and intraseasonal variability of the annual pressure wave at this time of the year.

Comparing the mean magnitudes of the Control winds for the June-July-August quarter with those for the same period of Year 9 of the GCM-data set (Figs. 16, 17) we find them in good agreement. The same must be true for the mean magnitudes of the pressure gradients. * On the other hand, the modeled vector mean winds are almost of the same size as the mean wind speeds while those observed are almost invisible. Observed daily wind vectors being of similar magnitude and relatively equally distributed over the full directional range cancel one another effectively and nearly vanish in the mean. Conversely, the small difference between modeled vector mean winds and mean wind speeds reveals the temporally invariant character of the modeled wind direction. In other words, a pressure pattern is required to be highly persistent, if not only the *mean magnitudes* of the winds but also the *vector means* of the winds (and accordingly the average divergence **) are to

* The foregoing does obviously not hold for the Greenland area. Conditions in this region are critical with regards to the outflow of ice from the Arctic Basin. So much the worse is it to realize that sea level pressure can only be obtained here via some type of reduction method. Such methods require arbitrary assumptions regarding orography and temperature variations in the imaginary air layer between surface and sea level. Especially the resultant too strong winds polewards of Greenland's northern tip appear to suffer from this.

** This bears the simple rule that a displacement is most efficient when it occurs along a straight line in response to unidirectional forcing. Moving zig zag and back and forth

take on large values.

As a consequence, the observed vector wind field is fairly indistinct whereas the simulated field takes on clearly structured shapes. The most dominant feature of the latter is the cyclonic flow pattern associated with a giant low pressure system centered over the Asian side of the Arctic Basin. This cyclone can establish sometimes as early as in May and may last through September. The ice underneath is forced to revolve in the same sense and is pulled apart on account of the divergent character of such flow. This can be verified from Fig. 18 which exhibits geographical distributions of $\nabla \cdot \vec{V}_{ice}$, the persistence of \vec{V}_{ice} , and the resulting ice compactness of August.

Excessive melting due to an enhanced gain of radiative energy over dynamically increased open water areas is the dominant process in Region III. In addition to this advective removal of ice becomes an essential factor in Region II. In this transition zone between Asian Low (1020 hPa) and Greenland High (1040 hPa) the ice drifts at velocities as high as 30cm/s. Some of this ice is saved from melting. Before this ice can exit the basin through the Fram Strait it is subjected to heavy ridging in front of this bottle neck. This leads locally to high values of thickness in excess of 10m.

In summary, a combination of two processes, namely the accelerated melt due to a persistently diverging ice drift and high speed ice export is what eventually leaves an ice free Central Arctic ocean behind.

5 Outlook

When driven with GCM-generated fluxes and winds the sea ice model fails to reproduce essential features of the Arctic ice cover. This failure is mainly caused by a wind forcing that is too vigorous and too persistent all year long. It is certainly possible to improve the model's performance via modifying the forcing components. However, it was never an objective of this research to establish a well performing *forced* model. Moreover, it is questionable if such modifications were particularly valuable in a coupled simulation.

We wish to conclude this report with some speculations on the potential of sea ice to modify the atmospheric circulation.

Ice-atmosphere feedbacks in Roeckner's coupled model employing static sea ice are relatively easy to predict. For instance, surface temperatures in continentally influenced sections of the Arctic - already low in the uncoupled GCM simulation - tend to drop farther. This is merely due to the fact that the conductive heat flux (usually a constant in uncoupled GCMs) is now taken to be inversely proportional to the *modeled* ice thickness. Hence, heavy ice conditions, as a rule, are closely related to very low surface temperatures in the case of static sea ice. The reverse applies to domains where relatively high temperatures are prevalent. Generally, the ice-atmosphere interaction in this model may well be suited to intensify the respective pressure field. It is however not believed that the overall structure of the atmospheric circulation in high latitudes could be affected extensively - unless the Arctic became ice free.

under a multidirectional forcing, on the other hand, may keep an ice floe essentially in place.

In a coupled simulation employing full ice dynamics this statement has possibly to be revised. The ice circulation will still be largely determined by the atmospheric wind field. As in the uncoupled Interannual Experiment the wind may again cause the ice to pile up in areas - and this is the important point - where thermal conditions alone suggest relatively thin or even no ice at all (e.g. Region I and IV). Again reduced conductive heat fluxes will cause a drop in surface temperature. Subsequently, the atmospheric fluxes are compelled to adjust. Via modifying the surface climate ice dynamics may have some noticable impact on the atmospheric circulation pattern itself.

An essential fact here is that a dynamical sea ice model is capable of producing disharmonies by pushing ice under an unfitting atmosphere which is required to adapt itself to the new boundary condition. Static ice, on the contrary, finds itself most of the time in perfect harmony with the thermal state of the atmosphere.

The above described mechanism is expected to be the weaker the more unstructured or homogeneous thickness, temperature and circulation fields are. As a consequence, our coupled model is likely to depict the interaction somewhat more exaggerated as compared to a not existing coupled model with better resolved atmospheric dynamics.

More quantitative evaluations really require a coupled model simulation to be carried out.

While not yet completed, efforts to construct a coupled model are well underway. Work already done includes the construction of meridionally extended sea ice grids for both hemispheres (Figs. 19,20). Also, the area of the fragments the ice grid squares fall into when the spherical lat-long GCM grid is overlayed needed to be known in order to handle the flux transfer and temperature exchange in an energetically consistent way.

Currently, we are still involved with mainly technical problems as debugging and testing parts of the computer code. A first test simulation will shortly be carried out on a small super computer.

Acknowledgements

Prof. W. Hibler is specially thanked for placing his dynamic thermodynamic sea ice model at my disposal, for his continuous advice and valuable comments at various stages of this research, and for revising a draft of this report. Thanks are also due Dr. E. Roegner who was kind enough to provide the simulated atmospheric forcing together with his global Hamburg University GCM. This Research was carried out at the U.S. Army Cold Regions and Research Laboratory under a reimbursable ONR Grant through CRREL for the U.S. Army Research, Development and Standardization Group, U.K., under Contract No. DAJA 45-86-M-0293. Additional funding was provided by the Max-Planck-Institut fuer Meteorologie, F.R.G.. Finally, I would like to thank Prof. W. Hibler and Prof. K. Hasselmann for providing me with the opportunity to carry out this research and Dr. J. Comati and Mr. U. Weinberger for unraveling the red tape associated with the support.

References

- Alexander, R.C. and R.L. Mobley, 1976: Monthly average sea surface temperatures and ice pack limits on a 1 degree global grid. *Mon. Wea. Rev.* 104, 143-148.
- Biercamp, J., 1986: Prognostic sea surface temperature in an Atmospheric climate model. *WMO/ICSU WCRP Report No. 9*, 8.34-8.36.
- Hibler, W.D.III, 1979: A dynamic thermodynamic sea ice model. *J. Phys. Oceanogr.* 9, 815-846.
- Hibler, W.D.III, 1980: Modeling a variable thickness sea ice cover. *Mon. Wea. Rev.* 108, 1943-1973.
- Hibler, W.D.III, and K. Bryan, 1987: A diagnostic ice-ocean model, *J. Phys. Oceanogr.* 17, 987-1015.
- Manabe, S. and R.J. Stouffer, 1980: Sensitivity of a global climate model to an increase in CO_2 concentration in the atmosphere. *J. Geophys. Res.* 85, 5529-5554.
- Parkinson, C.L. and W.M. Washington, 1979: A large -scale numerical model of sea ice. *J. Geophys. Res.* 84, 311-337.
- Pollard, D., M.L. Batteen and Y.J. Han, 1983: Development of a simple upper-ocean and sea-ice model. *J. Phys. Oceanogr.* 13, 754-768.
- Roeckner, E., 1979: A hemispheric model for short range numerical weather prediction and general circulation studies. *Contr. Atm. Phys.* 52, 262-286.
- Walsh, J.E., W.D. Hibler III and B. Ross, 1985: Numerical simulation of Northern Hemisphere sea ice variability, 1951-1980. *J. Geophys. Res.* 90, 4847-4865.

FIGURE SECTION

GRID CONFIGURATION AND REGIONS

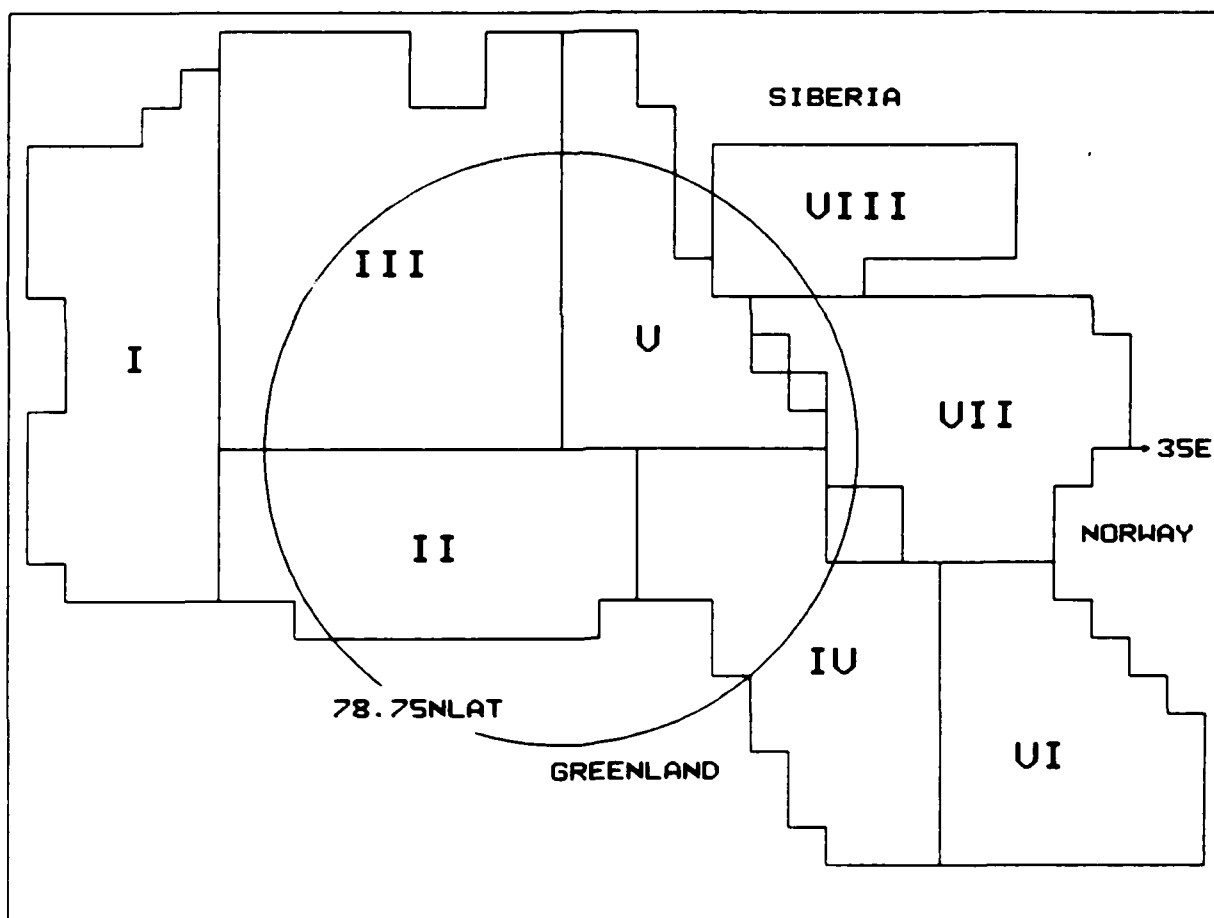


Figure 1: *Grid Configuration* as utilized for forced sea ice simulations. Roman numerals denote subregions defined for analyzing purposes. Dots mark cornerpoints of grid cells. $\Delta x = \Delta y = 160\text{km}$.

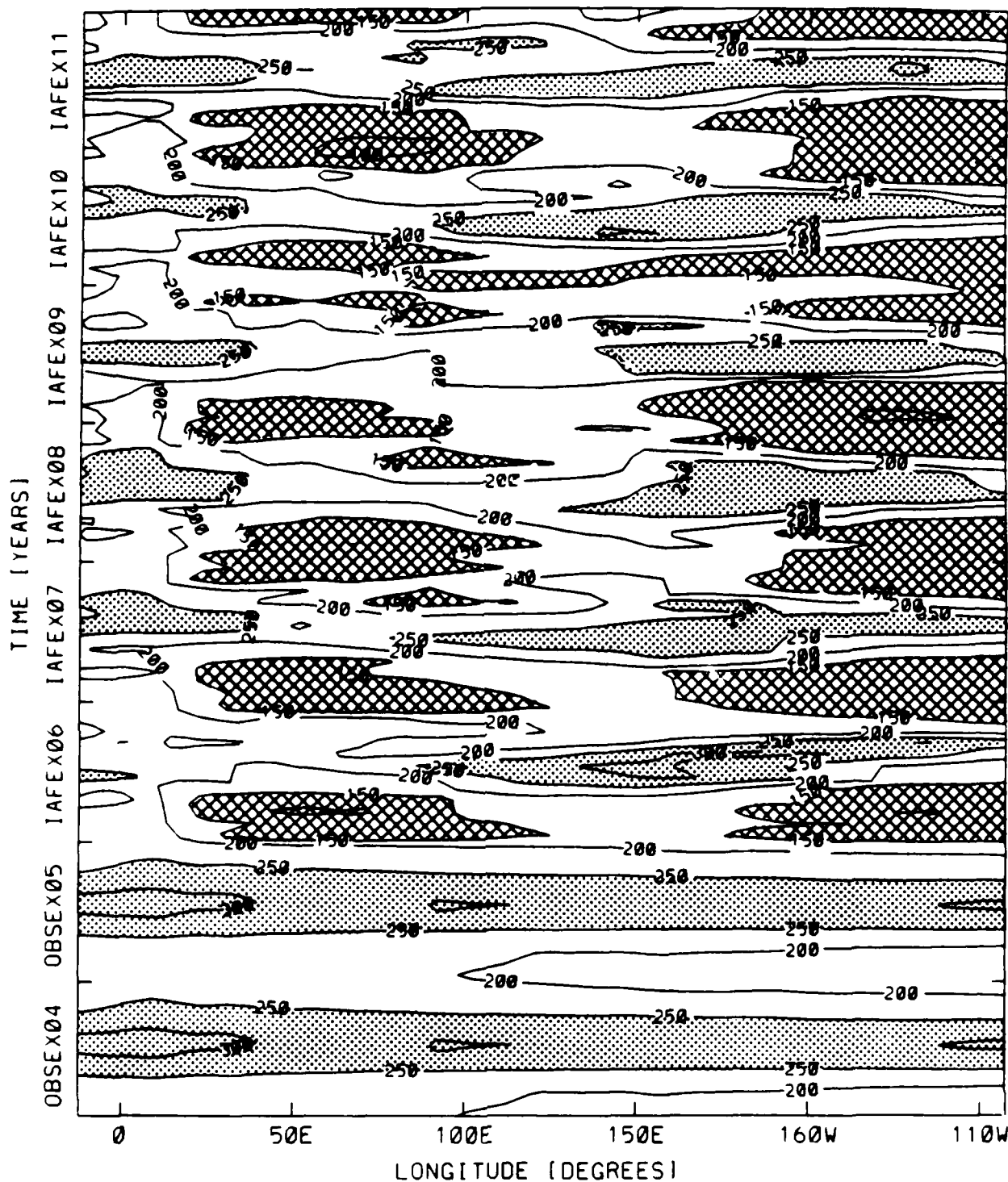


Figure 2: Time-longitude section along 78.75°N lat., showing incoming Longwave Radiation $W m^{-2}$ patterns. The complete GCM-generated data set (covering 6 years) is shown together with one year (obsex4=obsex5) of observational fluxes. These fluxes were utilized for the Interannual Forcing Experiment (IAFEX) and the Control Experiment (OBSEX) respectively.

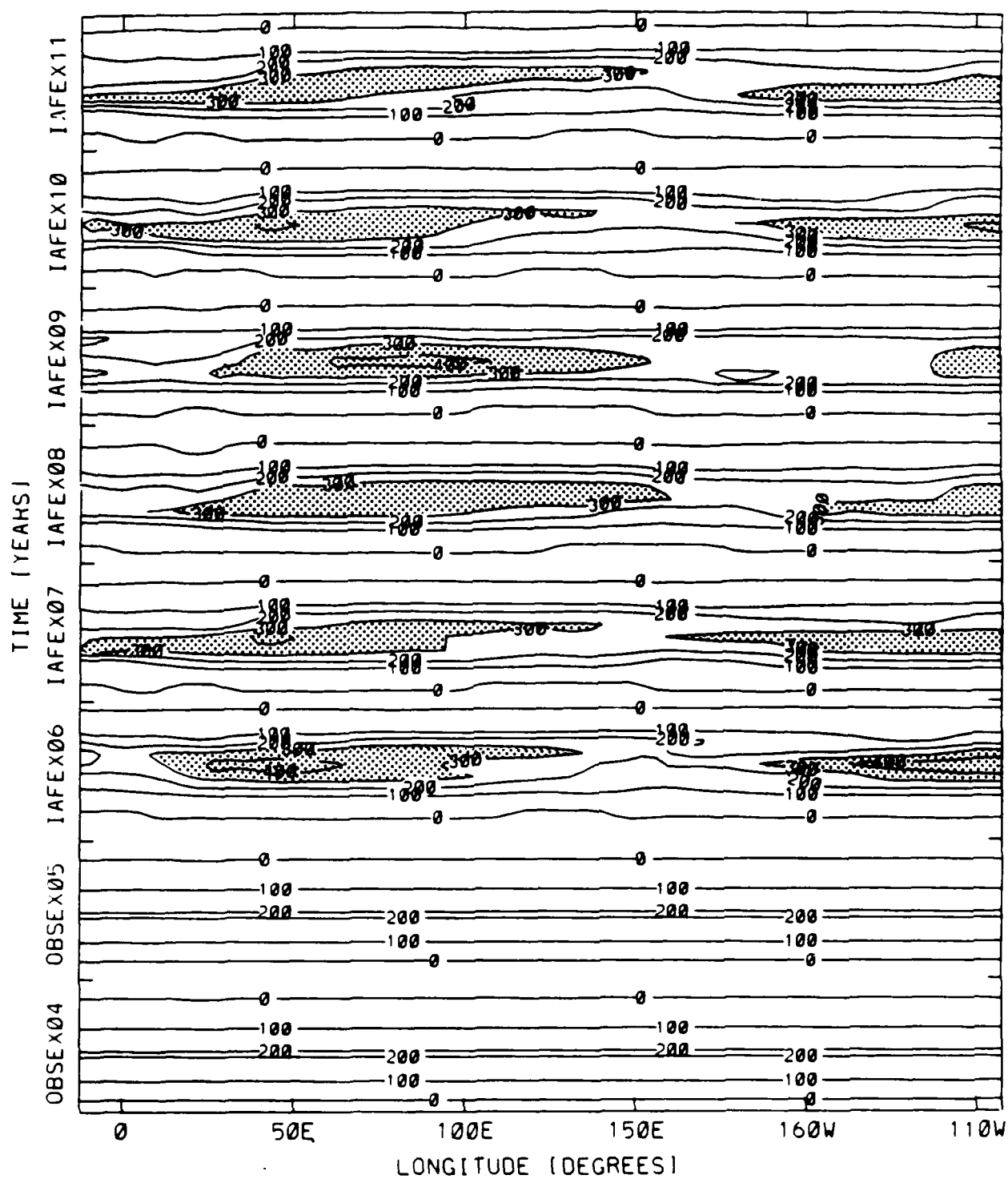


Figure 3: As in Fig. 2 except showing incoming Solar Radiation [W/m^2].

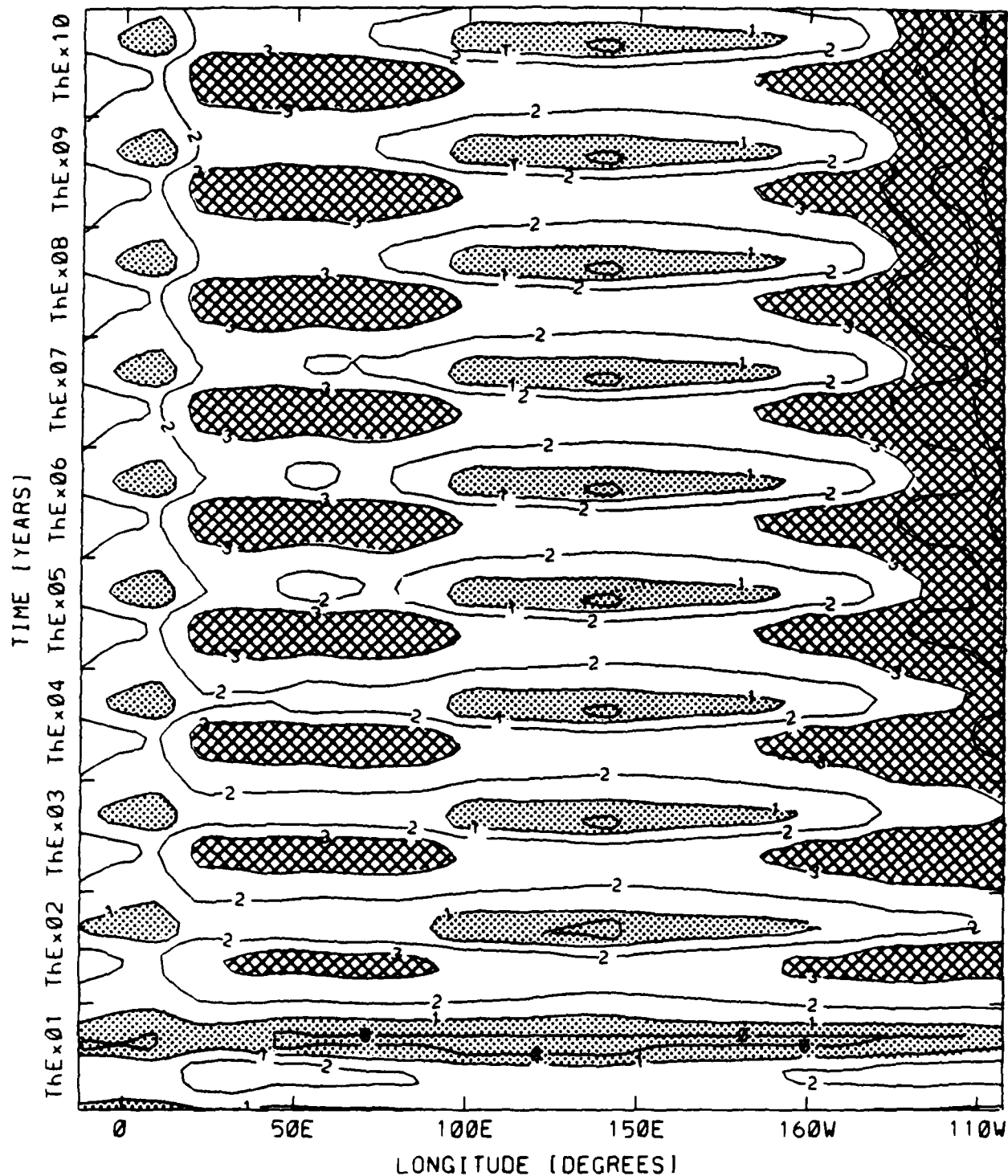


Figure 4: Time-longitude section along 78.75°N lat., showing *Ice Thickness [m]* patterns as produced with a Semtner-type thermodynamic sea ice model during an equiannual experiment repeatedly employing Year 6 of the GCM-forcing data set.

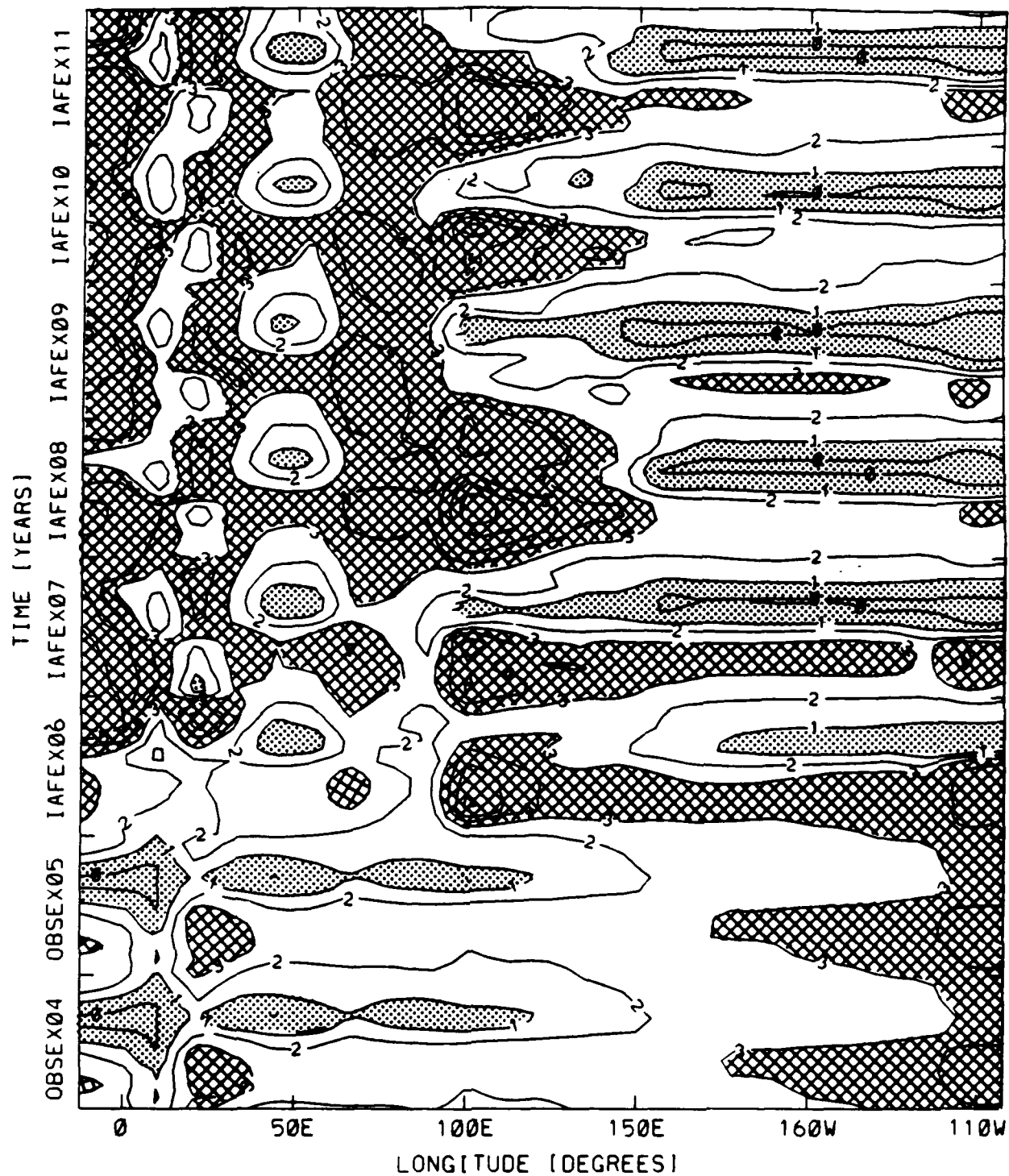


Figure 5 : Time-longitude section along 78.75°N .lat., showing *Ice Thickness [m]* patterns for the 4th and 5th year of the Control Experiment and for the Interannual Forcing Experiment.

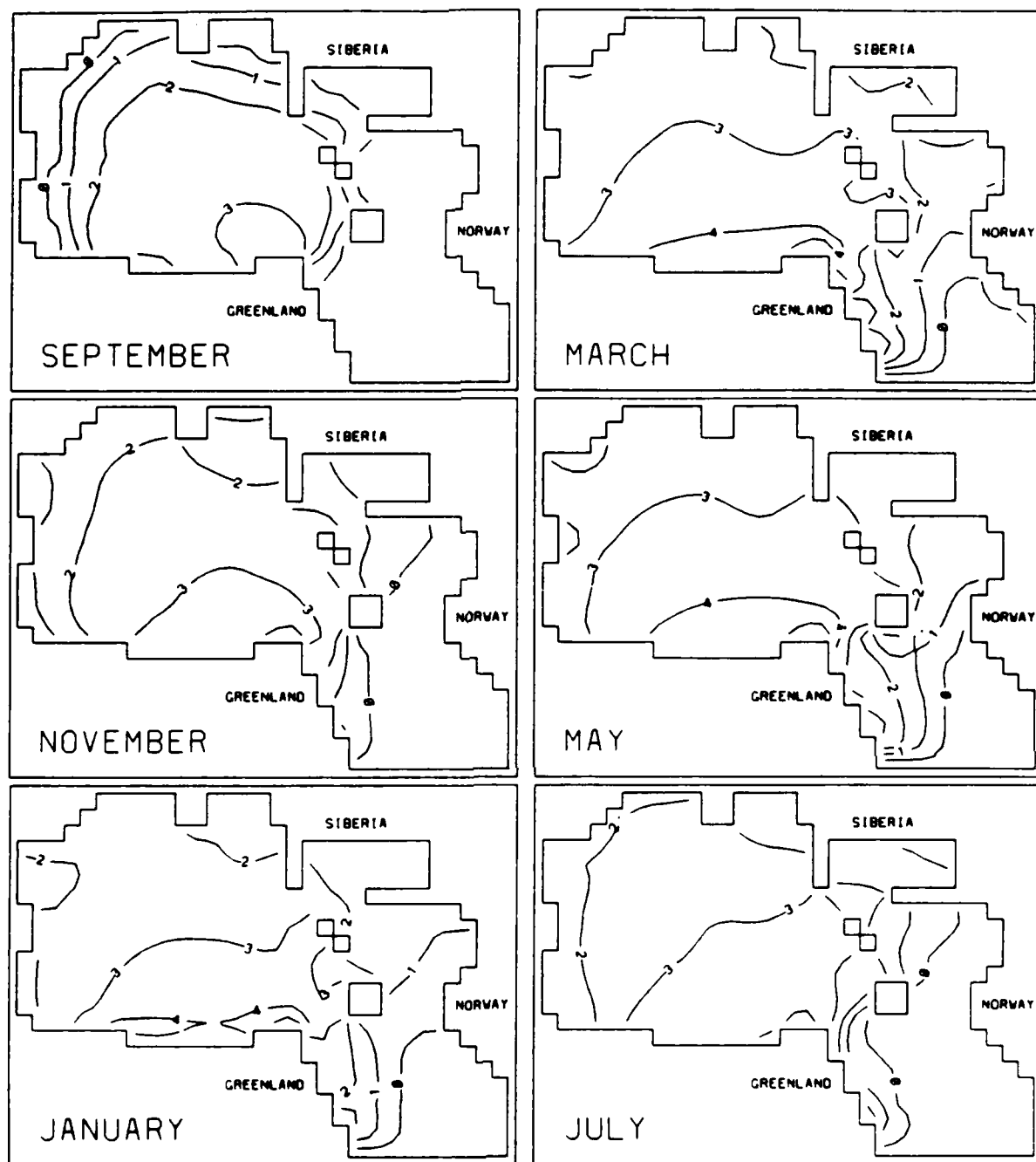


Figure 6: Geographical distribution of Ice Thickness [m] for every other month of the 5th year of the Control Experiment.

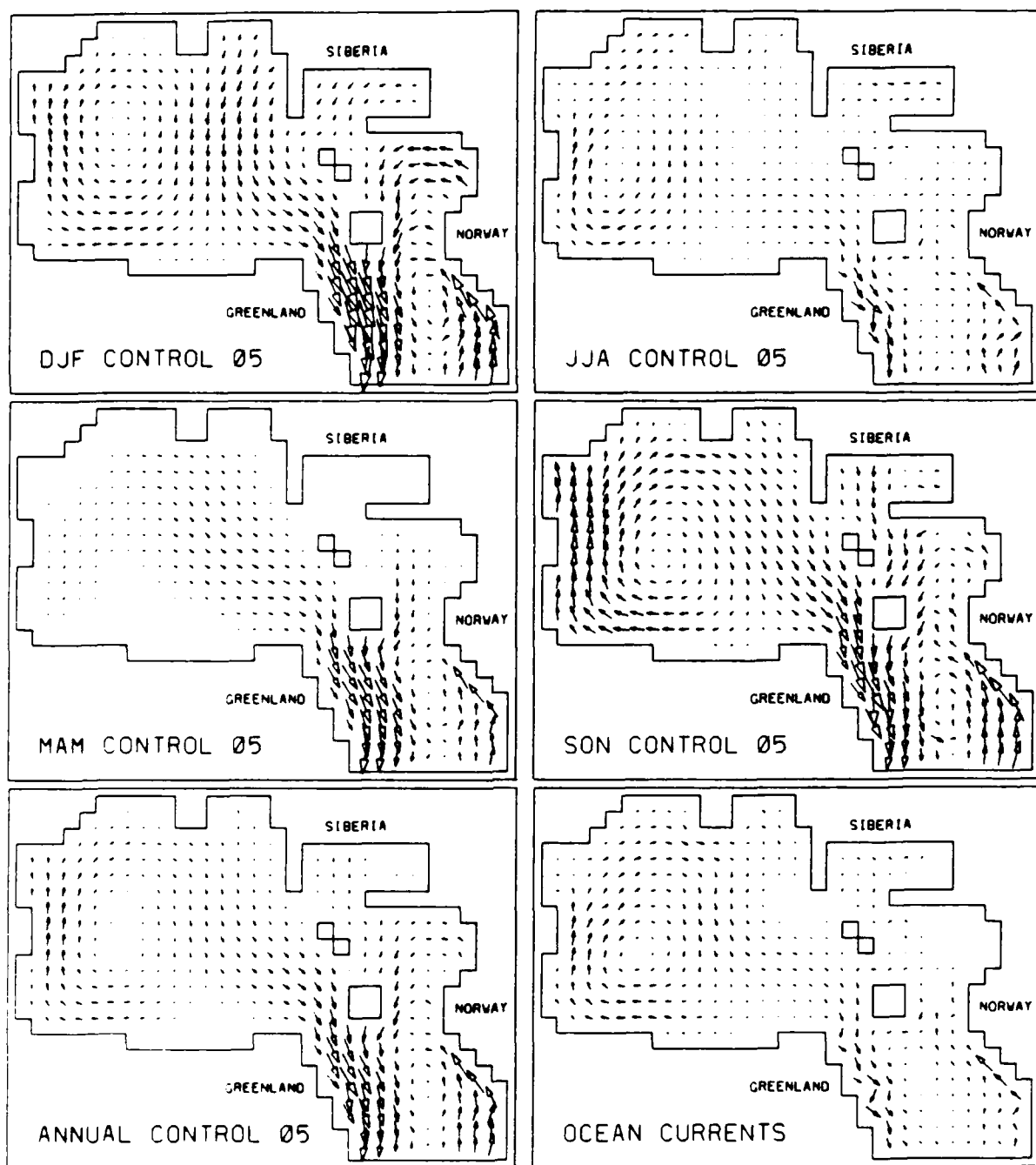


Figure 7: Seasonal and annual mean *Ice Drift* vectors for the 5th year of the Control Experiment and modeled annual mean *Ocean Currents*. Scale: one gridspace = 5cm/s.

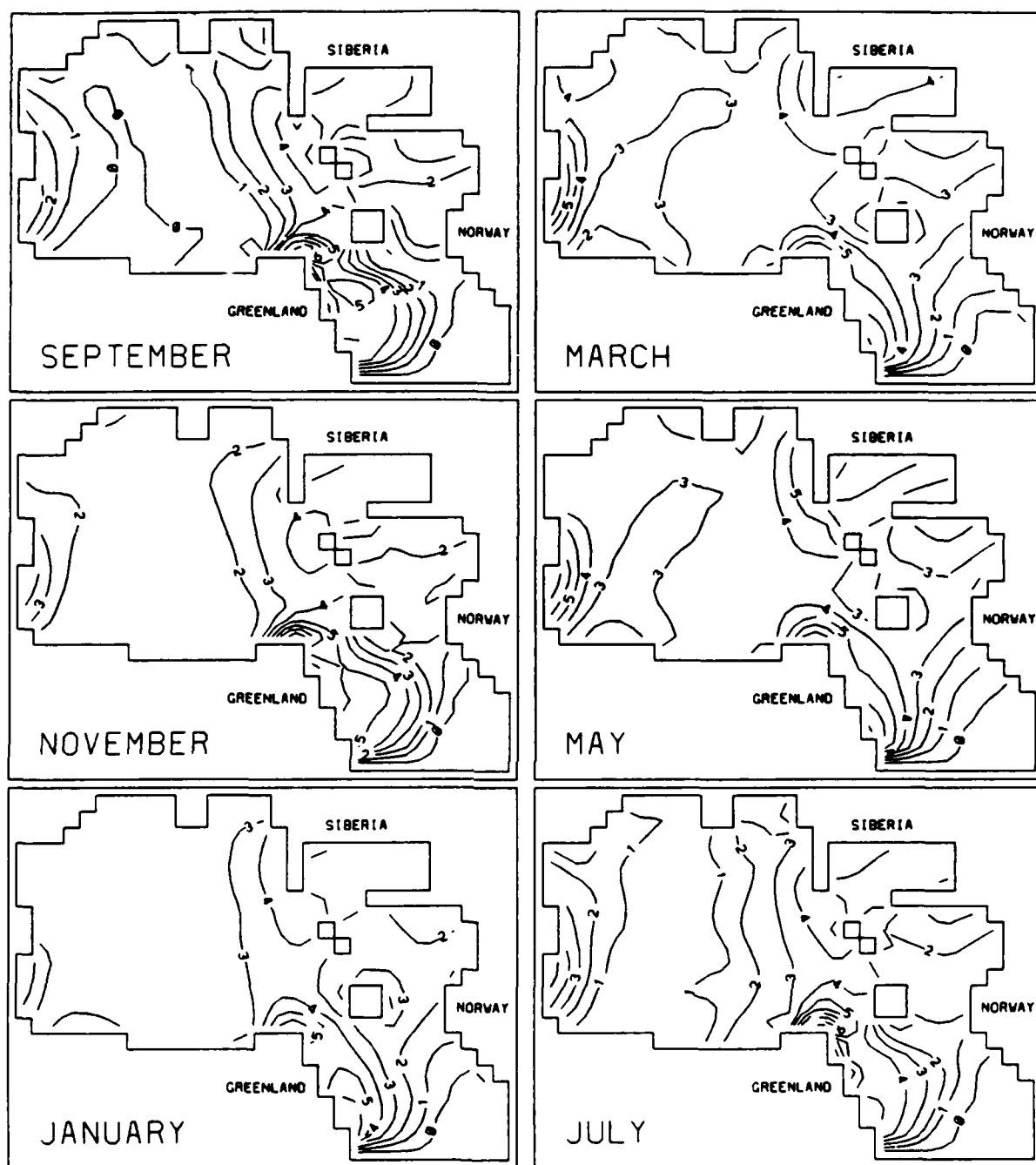


Figure 8 : Geographical distribution of the 6-year mean *Ice Thickness [m]* for every other month of the Interannual Experiment.

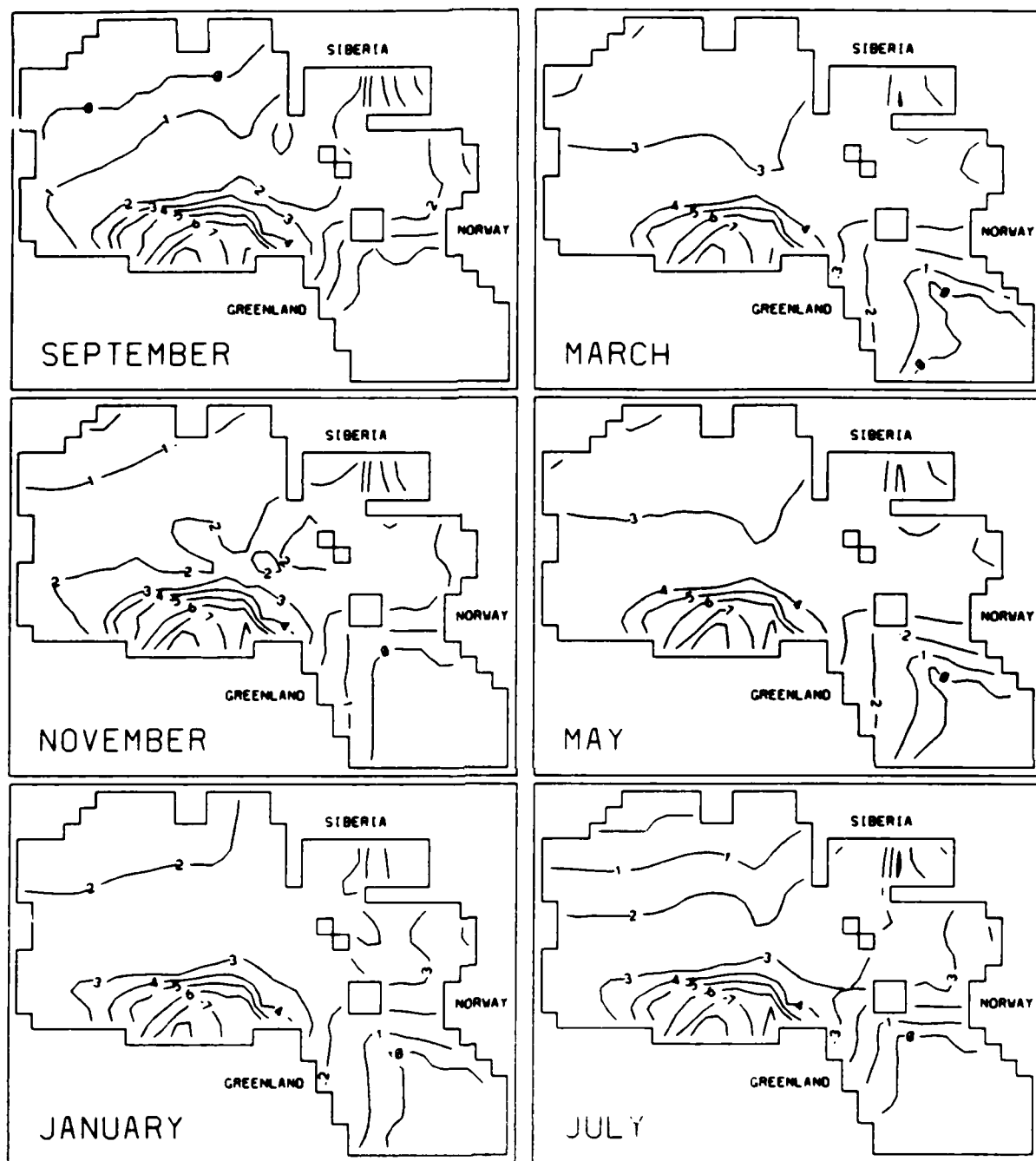


Figure 9: Geographical distribution of *Ice Thickness [m]* for every other month of the 10th year of an equilibrium simulation utilizing a Semtner-type thermodynamic sea model and Year 6 of the GCM-forcing data set (see also Fig.4).

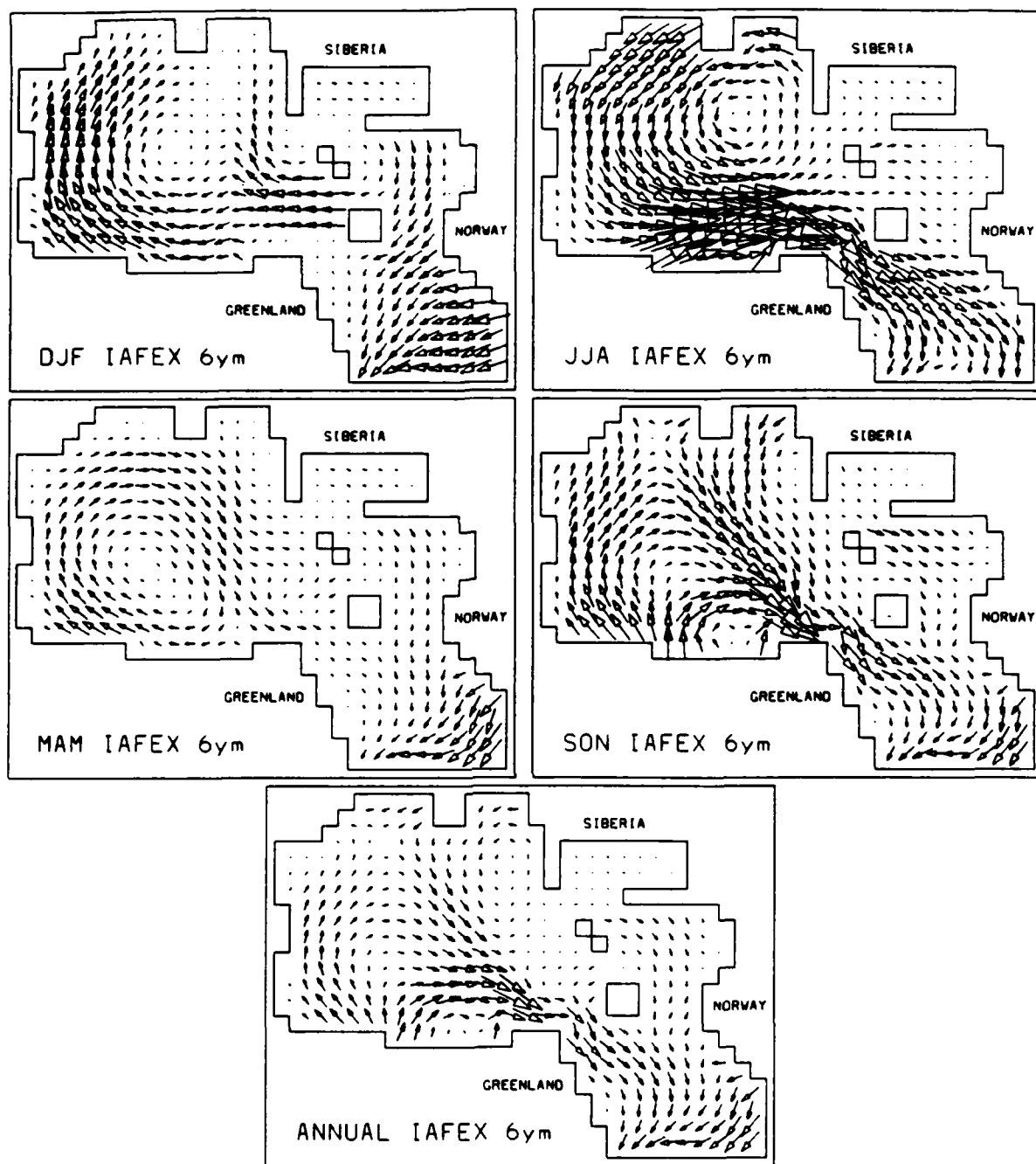


Figure 10 : 6-year mean seasonal and annual mean Ice Drift vectors as obtained from the Interannual Experiment. Scale: one gridspace = 5cm/s.

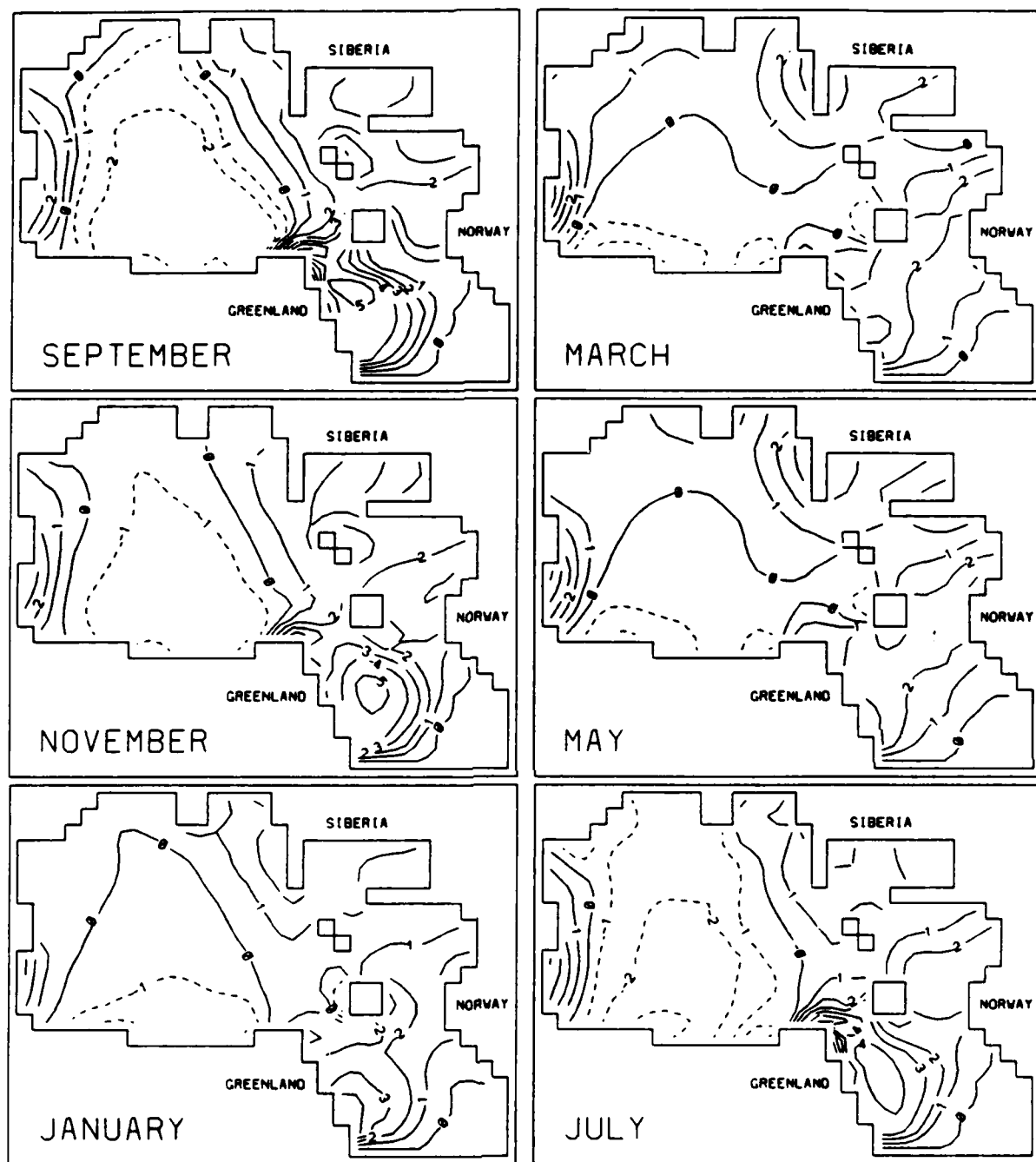


Figure 11 : Geographical distribution of Ice Thickness Differences $\Delta h \left(\doteq h(\overline{IAFEX}^{6y}) - h(C'ontrol^{y5}) \right) = \text{Fig. 8 minus Fig. 6}$ for every other month.

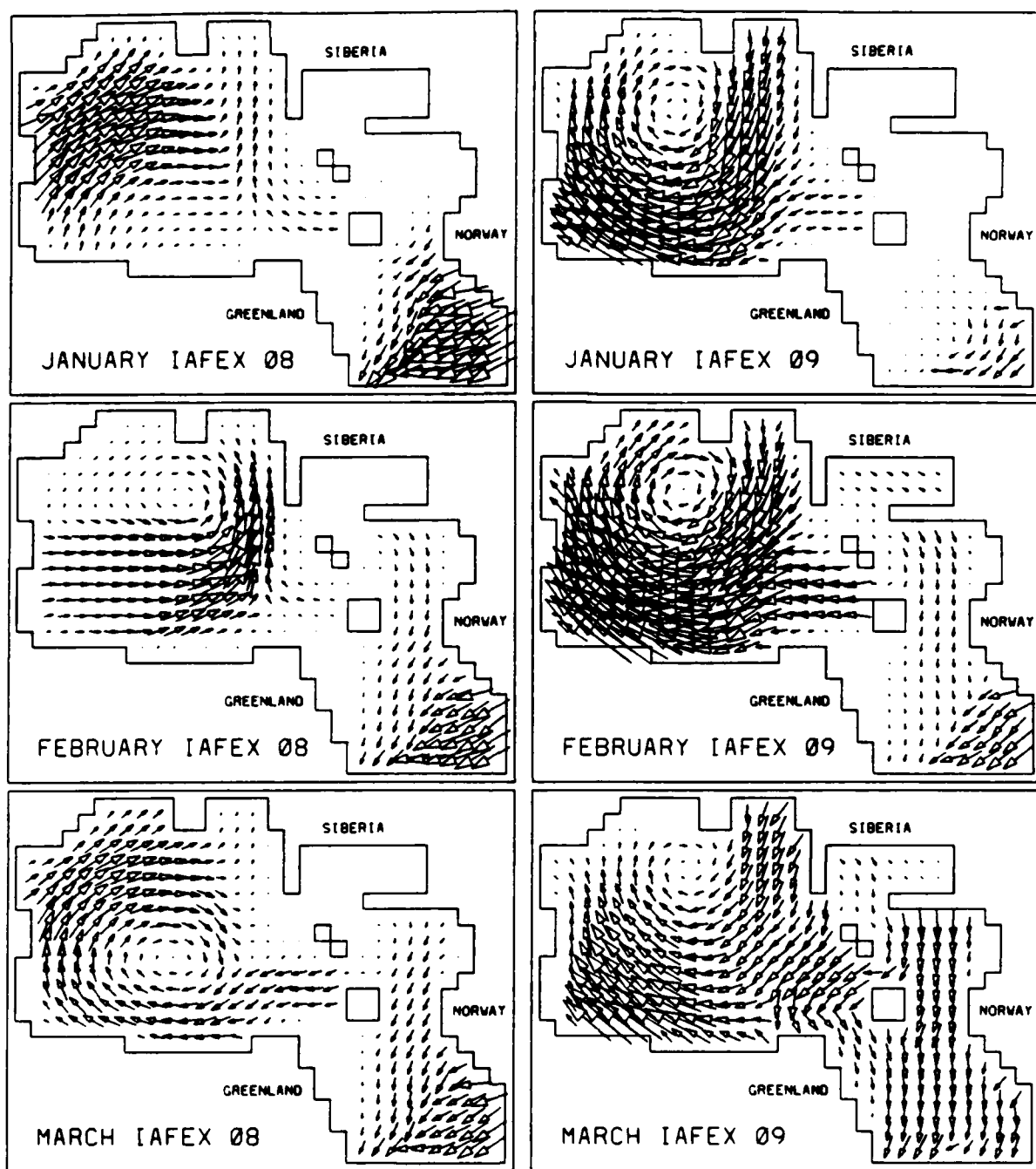


Figure 12 : Ice Velocity vectors for January, February, and March of Year 8 (left panel) and of Year 9 (right panel) of the Interannual simulation. One grid space represents a velocity of 5cm/s.

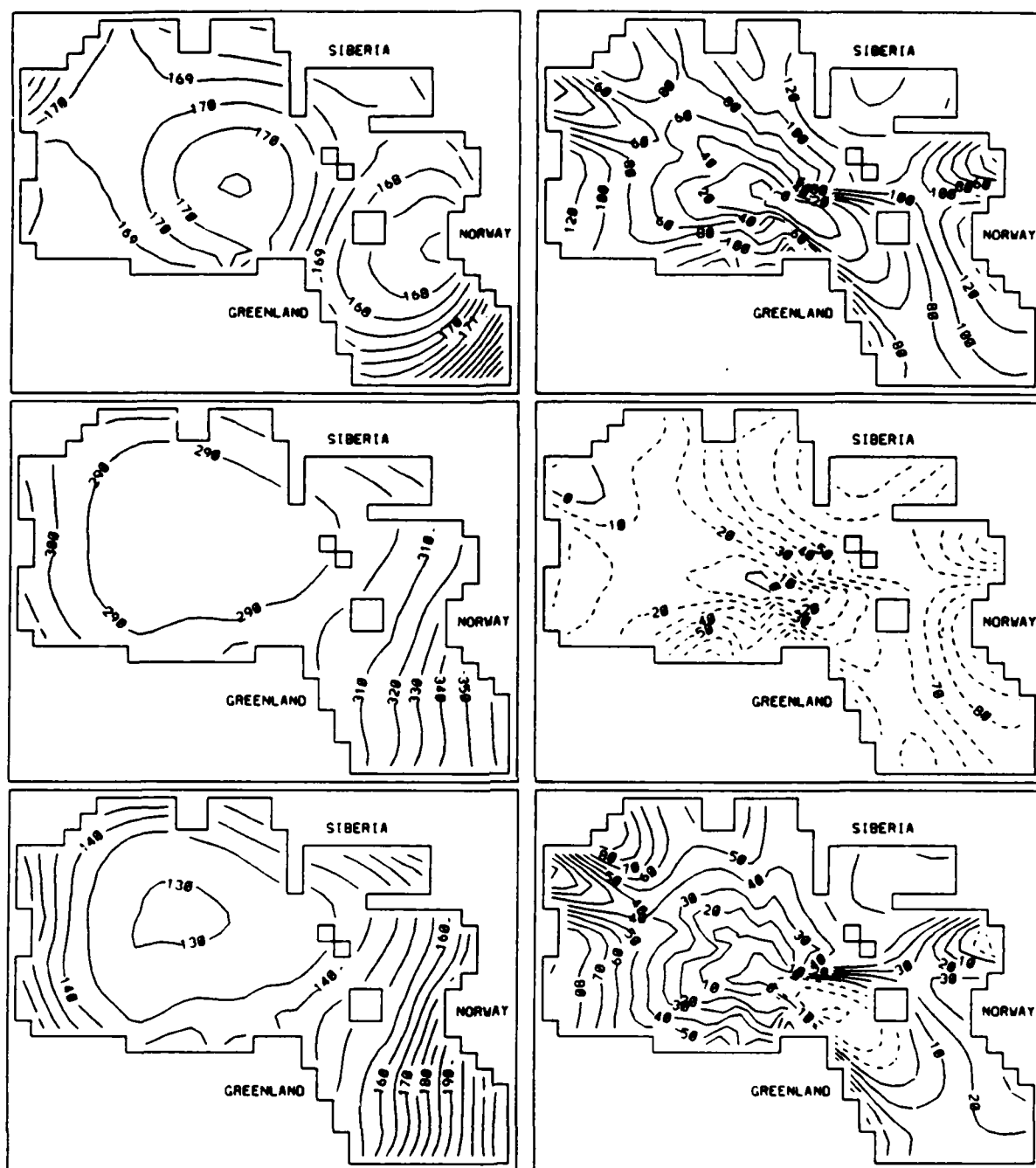


Figure 13 : *Surface Radiative Fluxes.* Upper left : frame depicts the geographical distribution of incoming Solar Radiation [W/m^2] utilized in the Control Experiment averaged over the JJA quarter. Middle left : same as in upper, except for incoming Longwave Radiation. Lower left : same as in upper, except for Total Net Radiation over open water (R_w). The surface reflects 10% of the incoming solar radiation and was assumed to radiate at the constant rate $\sigma \cdot 271.2^4$. This assumption leads to an overestimated net flux in ice free regions where the model allows the mixed layer to warm up. Right panel : same as in left panel, except depicting the difference: 6-year mean GCM-flux minus Control-flux.

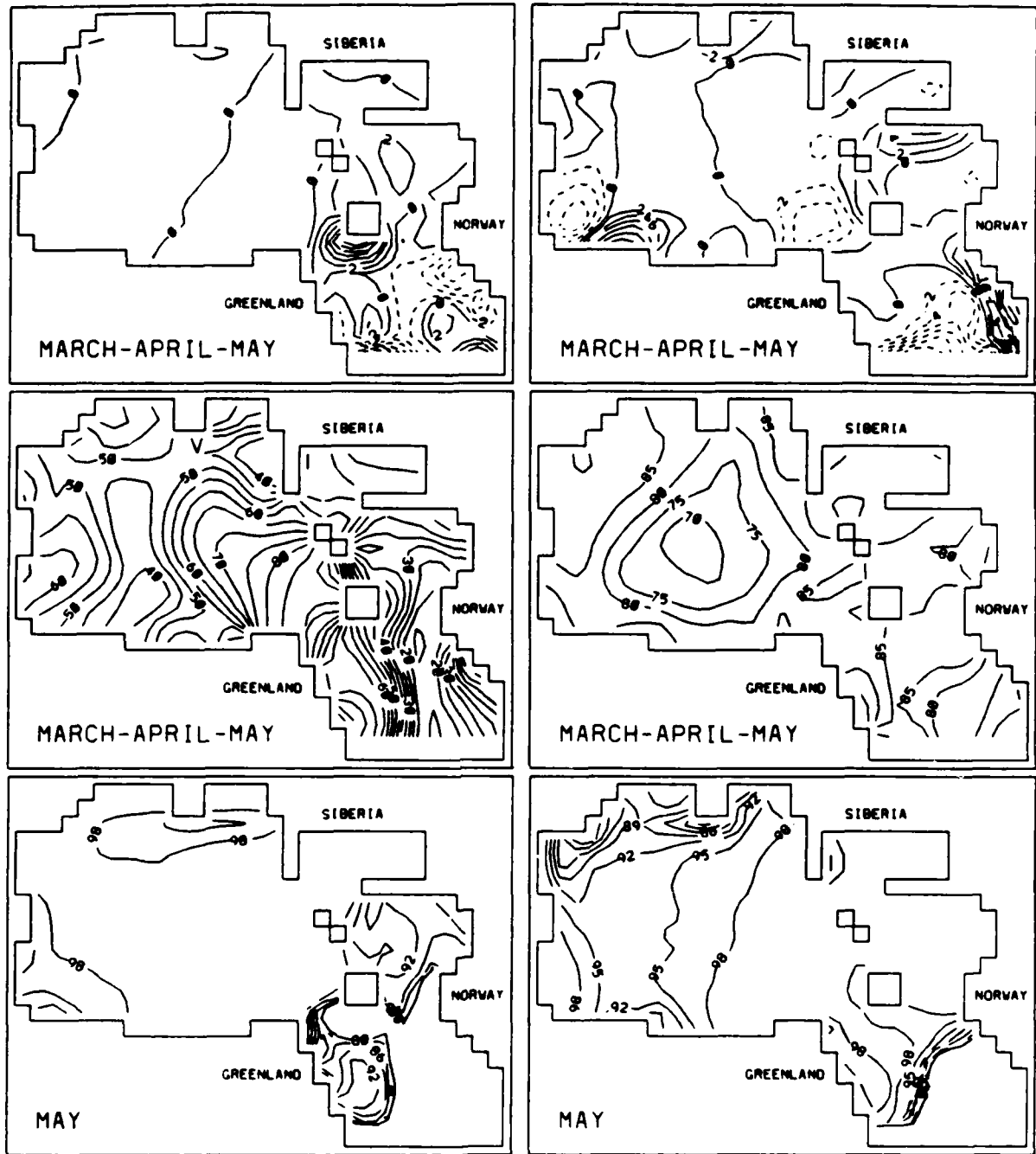


Figure 14: Divergence and Persistence of the ice velocity field during March-April-May and ice compactness in May. Upper left : frame depicts the geographical distribution of $\nabla \cdot \vec{V}_{ice}$ [$10^{-8} s^{-1}$] for the MAM period of the 5th year of the Control Experiment. Positive/negative labels denote lines of equal divergence/convergence. Middle left : same, except for Persistence [%] of \vec{V}_{ice} ($\hat{=} |\langle \vec{u} \rangle + \langle \vec{v} \rangle| \div |\langle \vec{u} + \vec{v} \rangle| \leq 1$). Lower left : same, except for Ice Compactness [%] in MAY (only the range $\geq 80\%$ is covered). Right panel : depicts corresponding 6-year average fields as obtained from the Interannual Experiment.

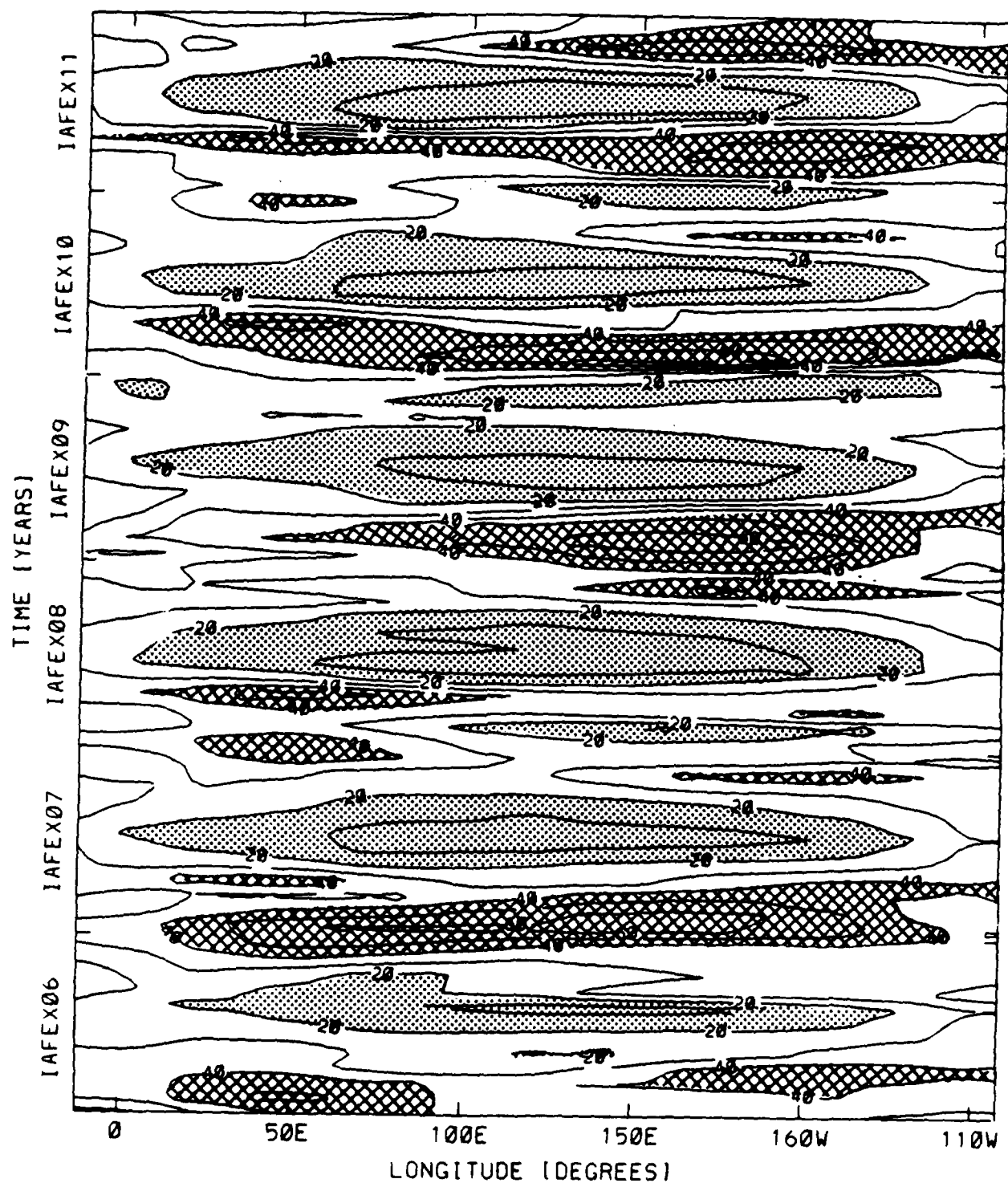


Figure 15 : Time-longitude section along 78.75°N lat., showing six years of GCM-generated Sea Level Pressure (hPa-1000). Corresponding observed pressure data were not at hand.

Figure 16 : Observed Geostrophic Winds, June-July-August mean. One gridspace represents a velocity of 10m/s. Given are:

- 1) the vectormean ($:= \langle \vec{u} \rangle + \langle \vec{v} \rangle$) by the arrow pointing away from the gridpoint,
- 2) the standard deviation from the vectormean ($:= \sqrt{s(u)^2 + s(v)^2}$) by the radius of the sector of a circle around the gridpoint,
- 3) the weighted average directional deviation of the velocity vectors from the direction of the vectormean A

$$\sqrt{\sum |\vec{u}_i + \vec{v}_i| * (\alpha_i - A)^2 / \sum |\vec{u}_i + \vec{v}_i|} \quad \text{with} \quad -\pi \leq \alpha_i - A \leq +\pi$$

by the arc the sector cuts out of 2π ,

- 4) the mean magnitude of the velocity vectors ($:= \langle |\vec{u} + \vec{v}| \rangle$) by the length of the arrow plus what exceeds it.

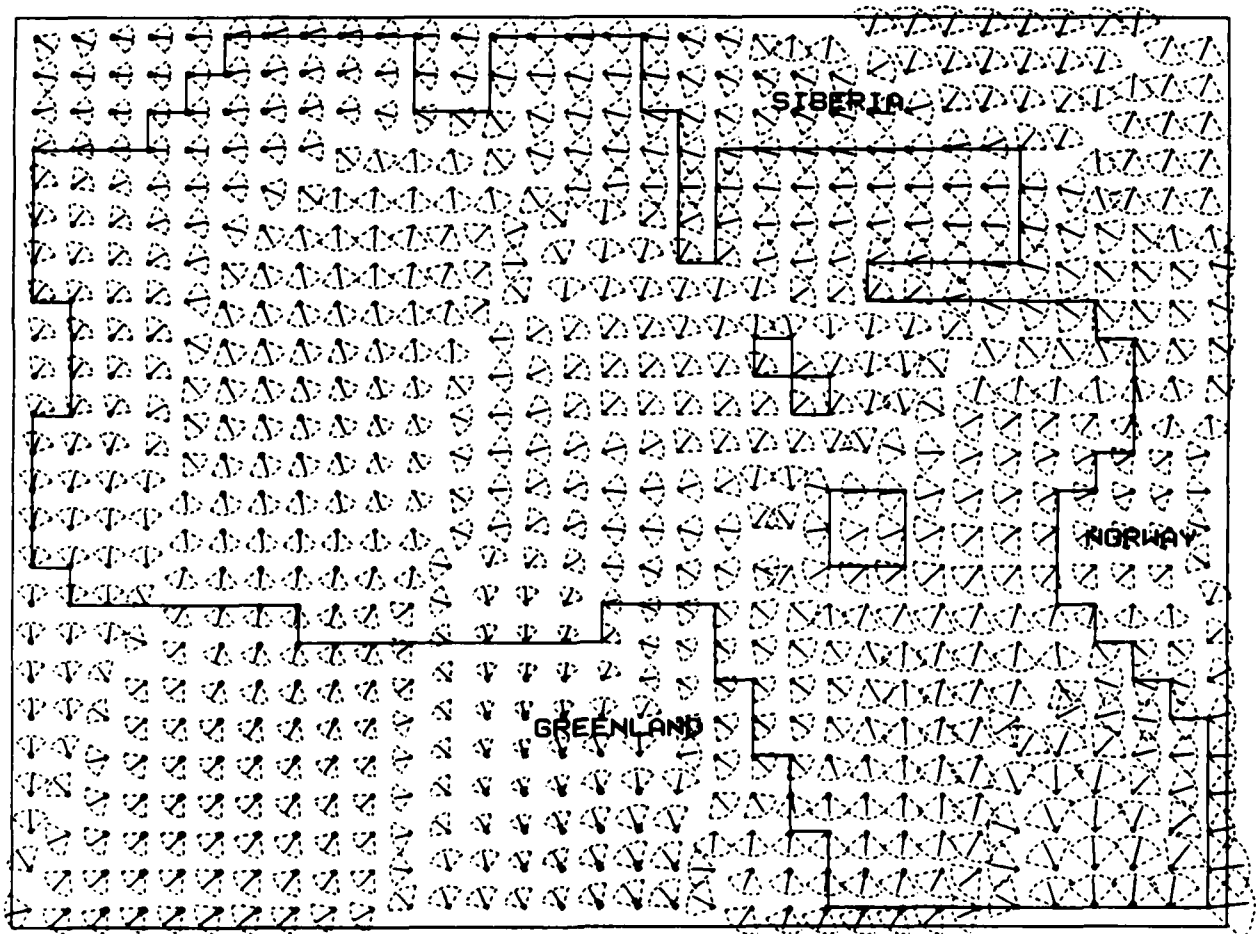


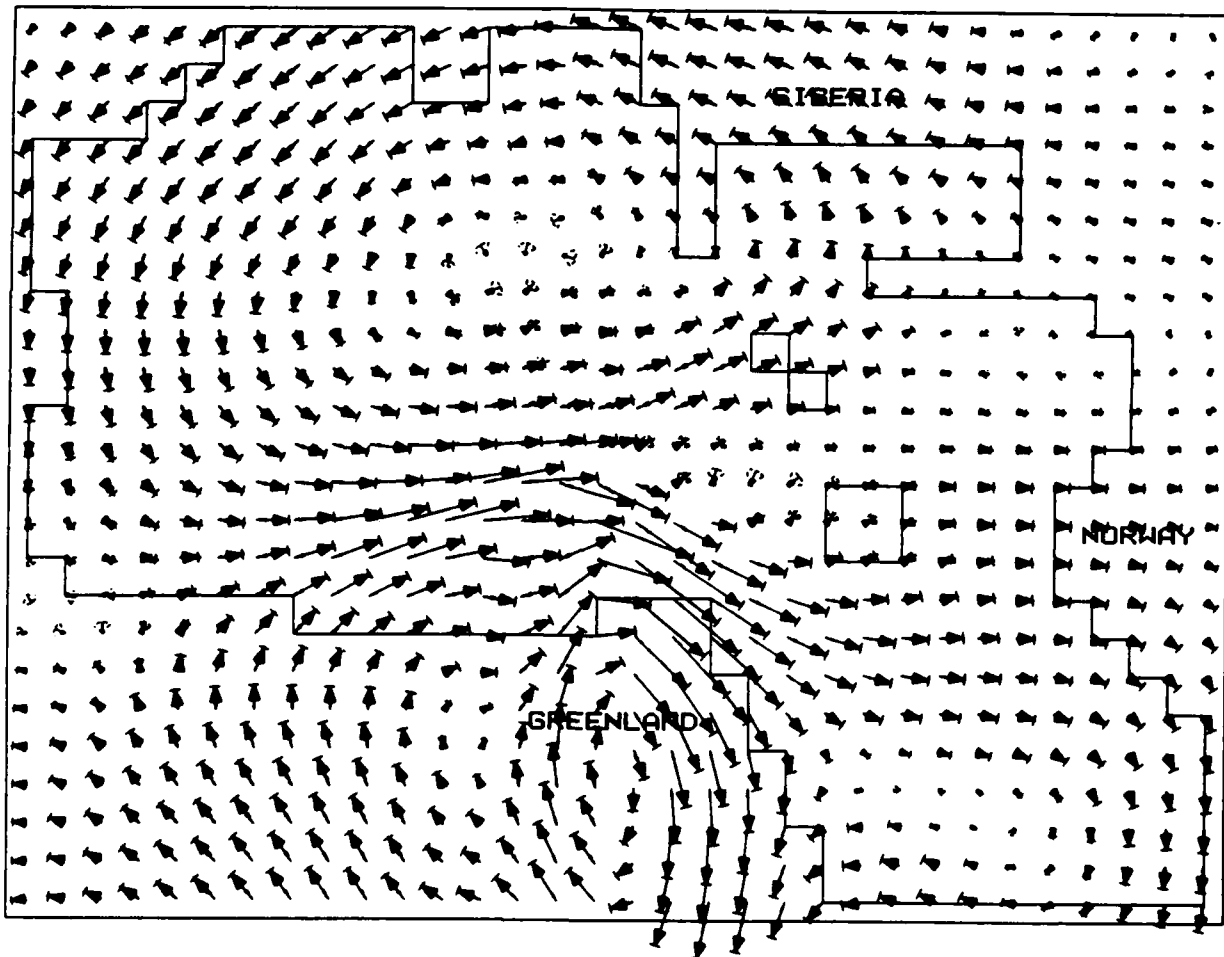
Figure 17 : *Modeled Geostrophic Winds*, June-July-August mean of Year 9 of the GCM-data set. One gridspace represents a velocity of 10m/s. Given are:

- 1) the vectormean ($:= \langle \vec{u} \rangle + \langle \vec{v} \rangle$) by the arrow pointing away from the gridpoint,
- 2) the standard deviation from the vectormean ($:= \sqrt{s(u)^2 + s(v)^2}$) by the radius of the sector of a circle around the gridpoint,
- 3) the weighted average directional deviation of the velocity vectors from the direction of the vectormean A

$$\sqrt{\sum \vec{u}_i + \vec{v}_i \cdot (\alpha_i - A)^2 / \sum |\vec{u}_i + \vec{v}_i|} \quad \text{with} \quad -\pi \leq \alpha_i - A \leq +\pi$$

by the arc the sector cuts out of 2π ,

- 4) the mean magnitude of the velocity vectors ($:= \langle |\vec{u} + \vec{v}| \rangle$) by the length of the arrow plus what exceeds it.



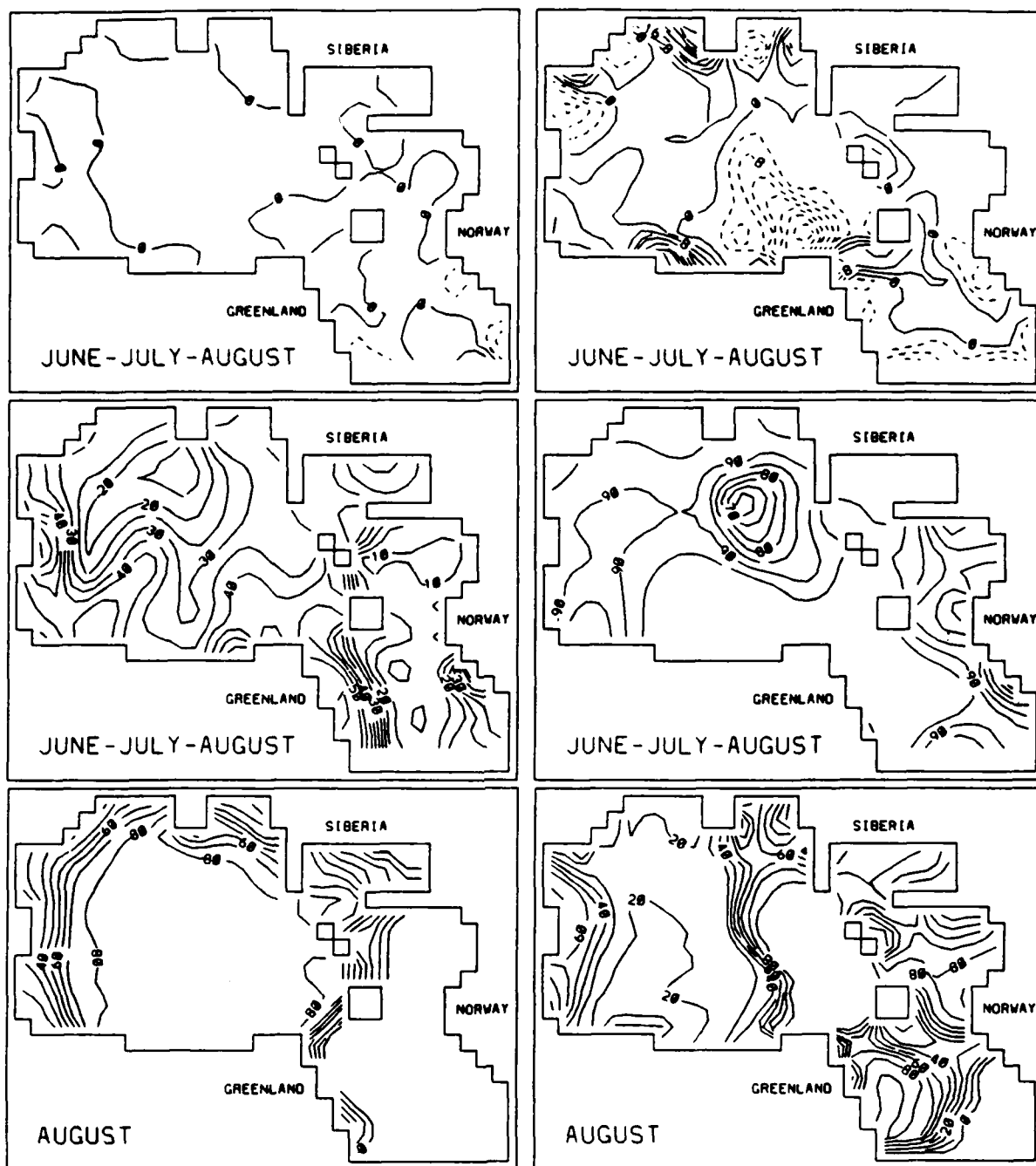


Figure 18: Divergence and Persistence of the ice velocity field during June-July-August and ice compactness in August. Otherwise as in Fig. 14. However, note that the contour interval for the divergence frames (top) is increased by a factor 2 and that ice compactness (bottom) is depicted over the full range here.

LAMBERT AZIMUTHAL EQUAL AREA PROJECTION

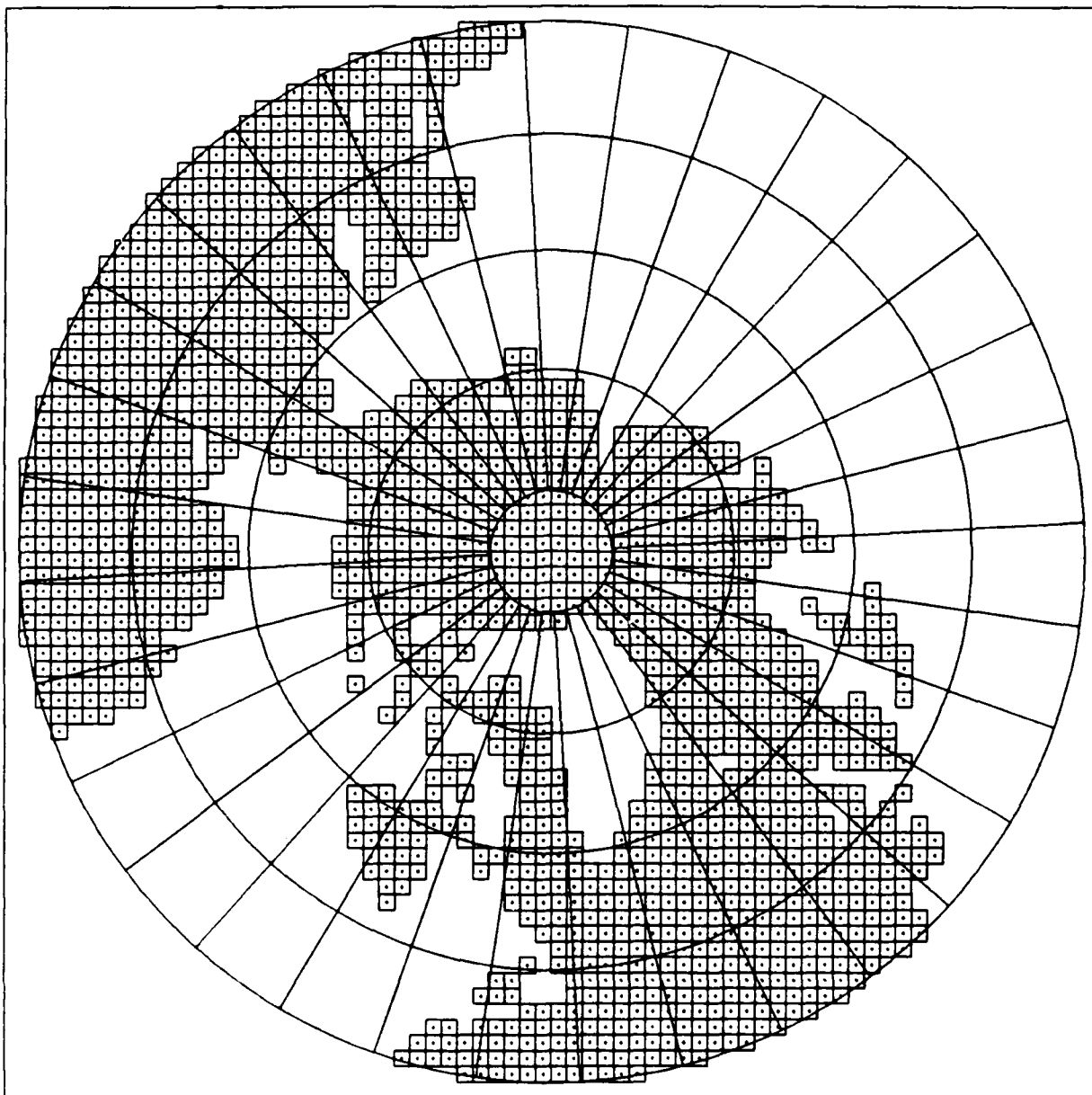


Figure 19 : Northern Grid Configuration to be utilized for global coupled air-ice simulations. Dots mark centers of ice grid cells of the size $\Delta x = \Delta y = 160\text{km}$. The horizontal resolution of the GCM is $\Delta\lambda = \Delta\phi = 11.25^\circ$. Atmospheric grid points are defined at the centers of the depicted lat.-long. sectors.

A circular diagram with a central circle, radial lines, and concentric rings, overlaid with a grid of small squares. The diagram is composed of a central circle, a series of concentric circles, and radial lines extending from the center to the outer edge. A grid of small squares is overlaid on the entire circular area, with the squares being more densely packed in the outer regions. The diagram is enclosed within a square frame.

APPENDIX A

Graphical Documentation of Mass Budget

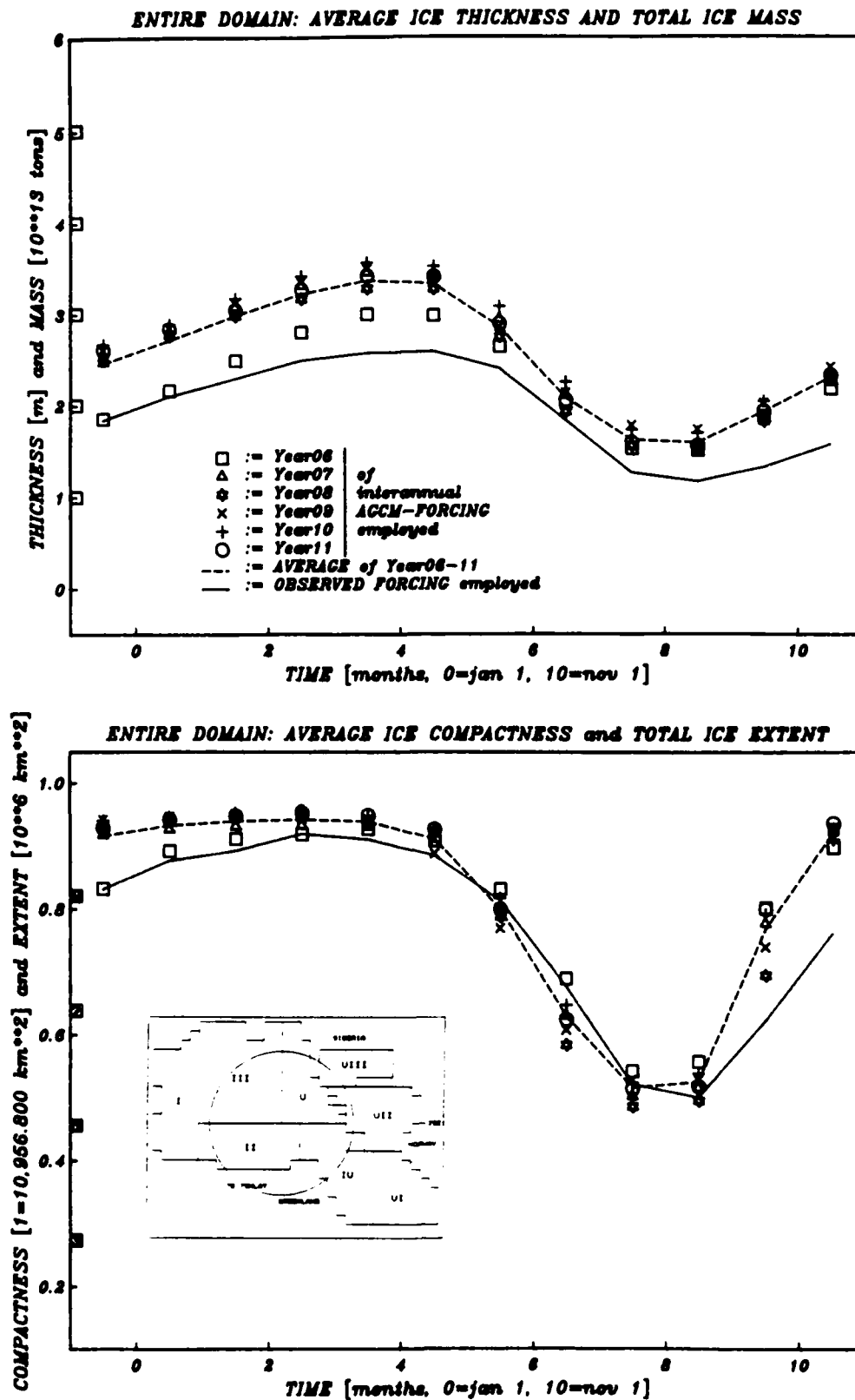


Figure A0 : Annual cycles of monthly and over the entire grid domain averaged *Ice Thickness* and *Ice Compactness* for the Control and the Interannual simulation. Boxed values at the inner side of the ordinate give the ice mass and the ice covered area respectively.

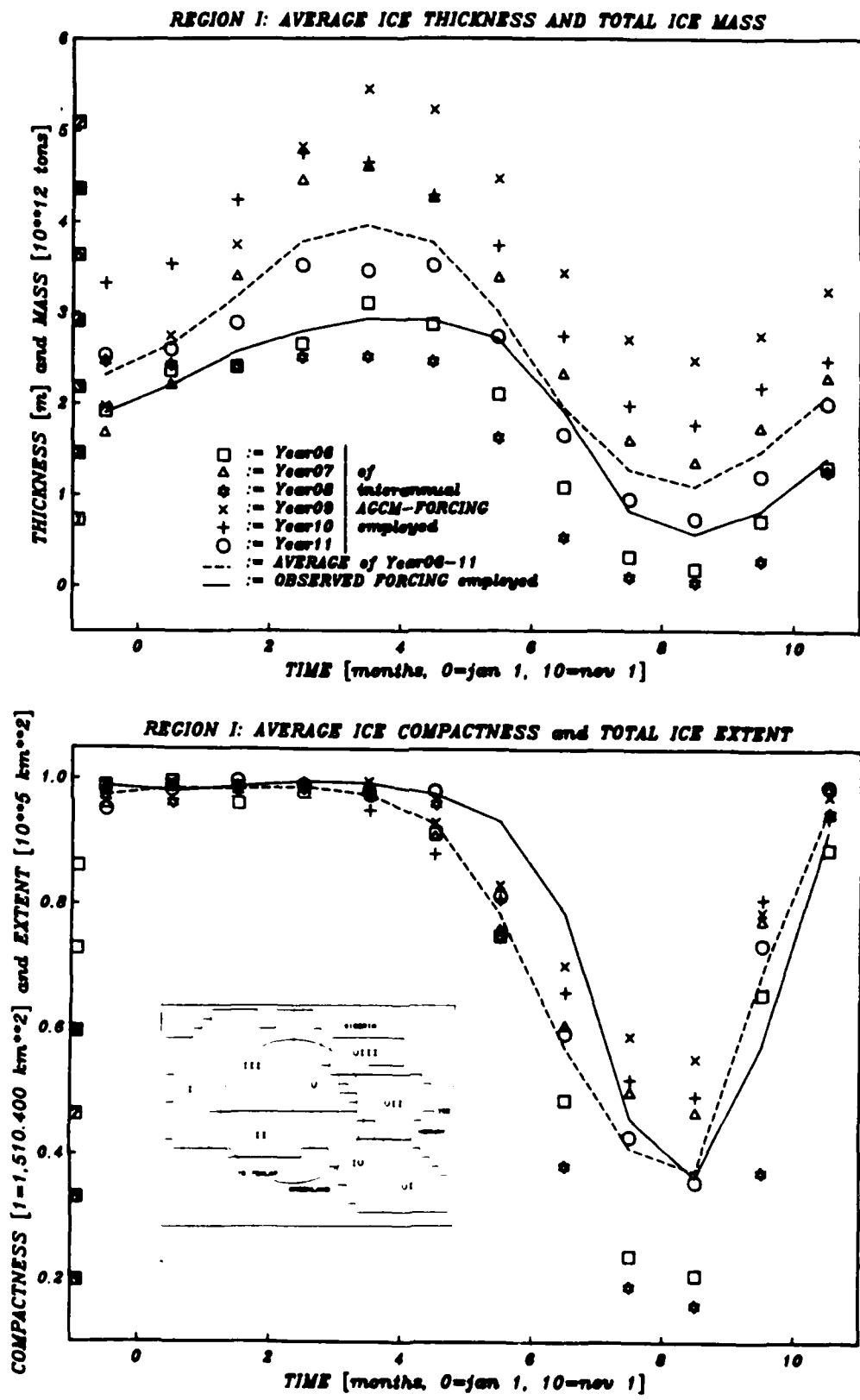


Figure A1 : As in Fig. A0 except for Region I (Bering Strait).

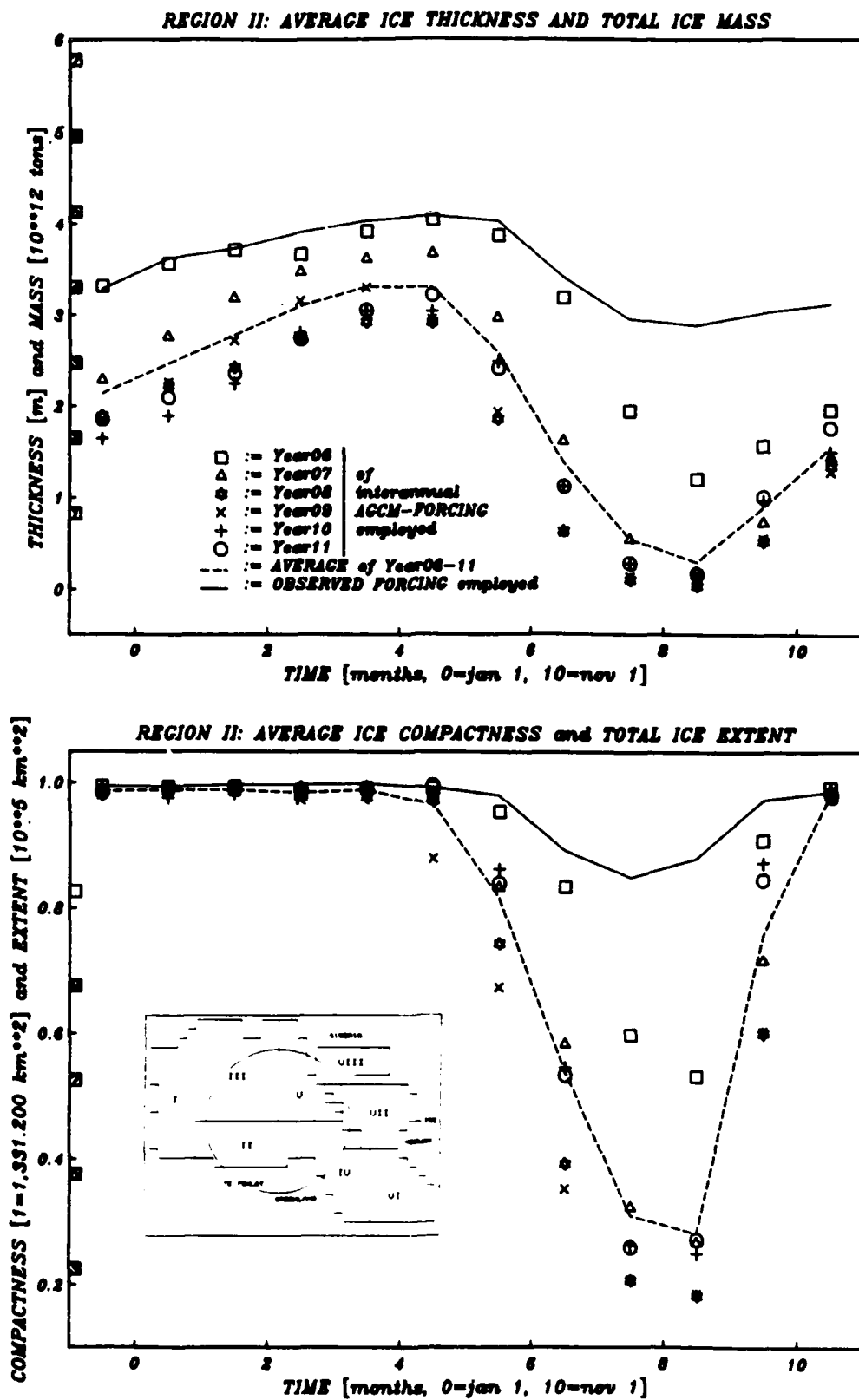


Figure A2 : As in Fig. A0 except for Region II (Canadian Arctic).

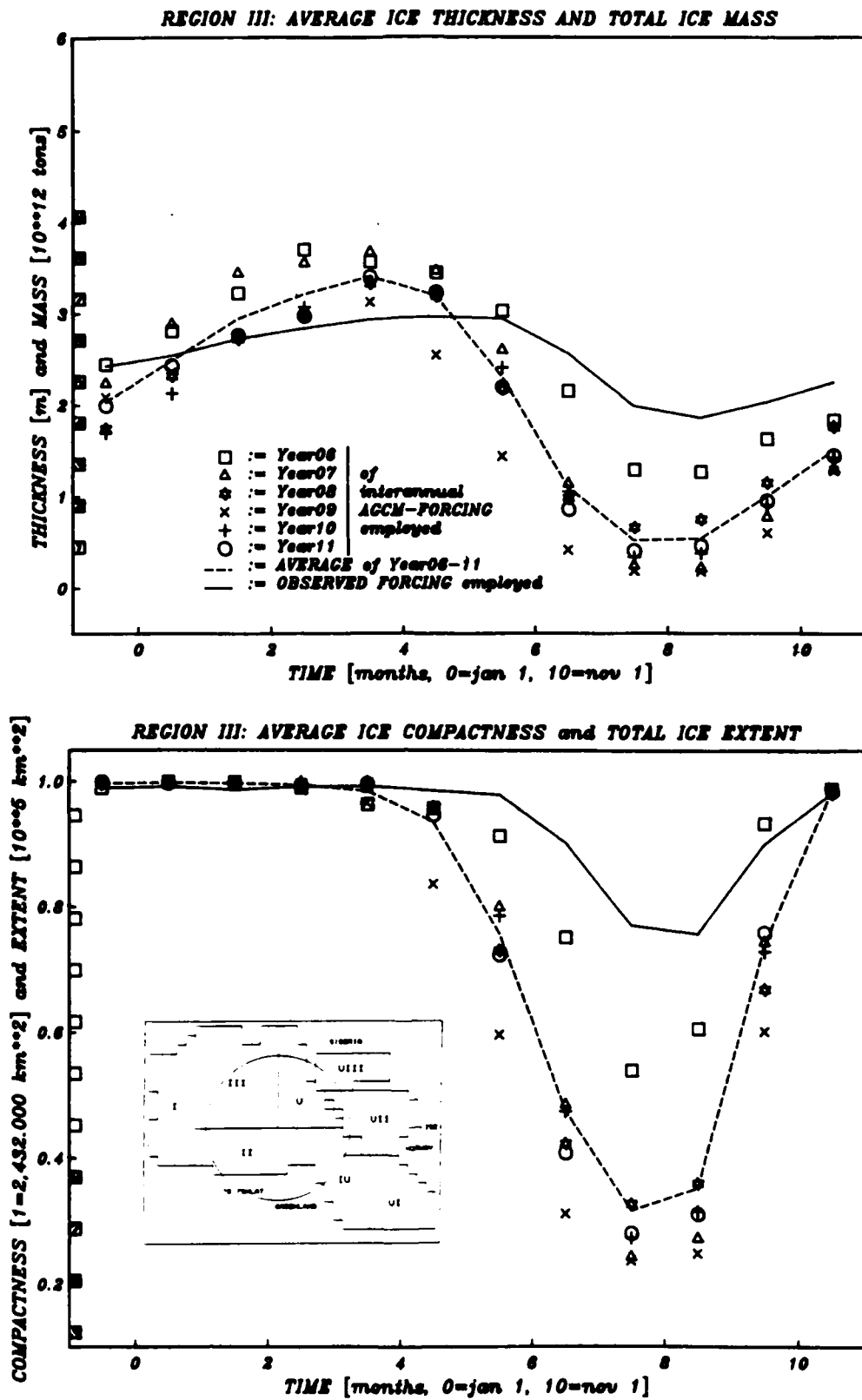


Figure A3 : As in Fig. A0 except for Region III (Central Arctic).

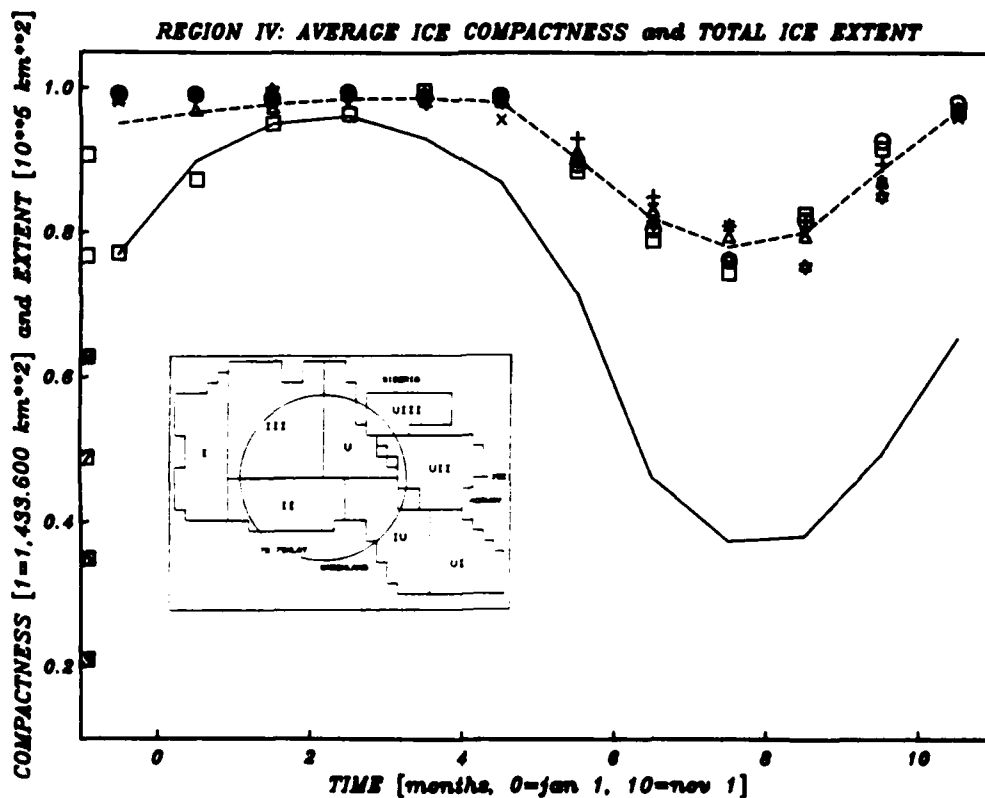
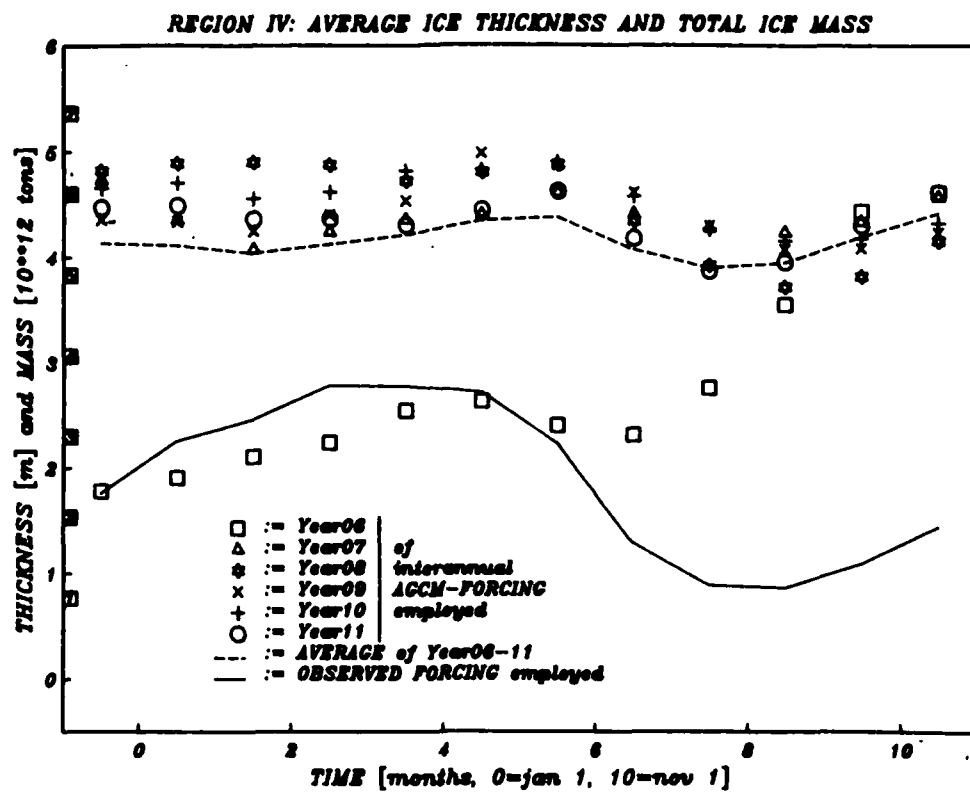


Figure A4 : As in Fig. A0 except for Region IV (East Greenland Sea).

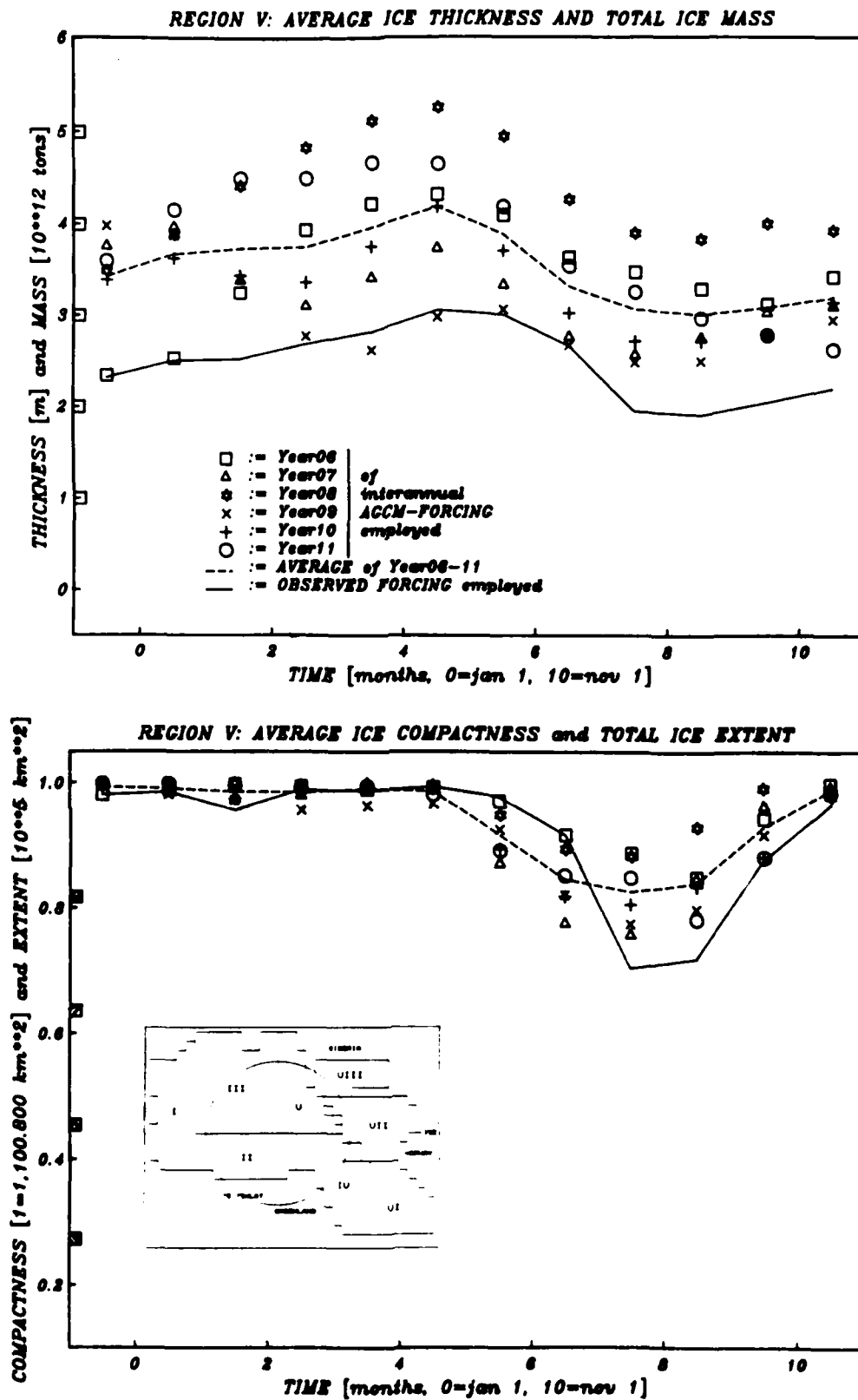


Figure A5 : As in Fig. A0 except for Region V (Laptev Sea).

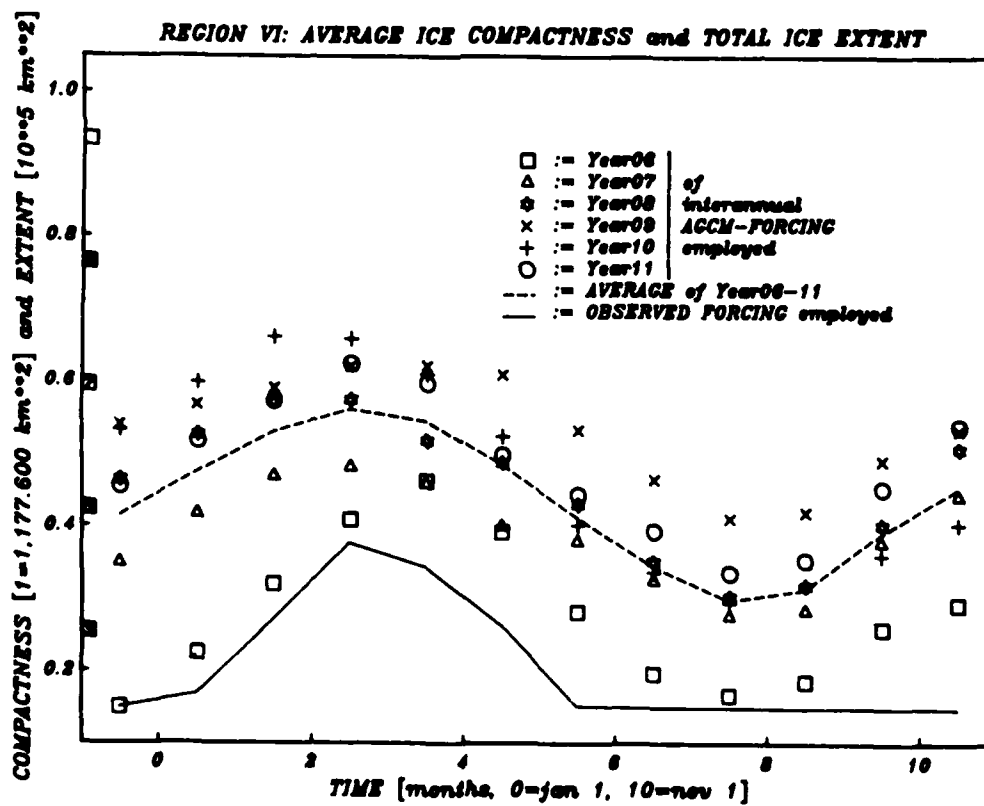
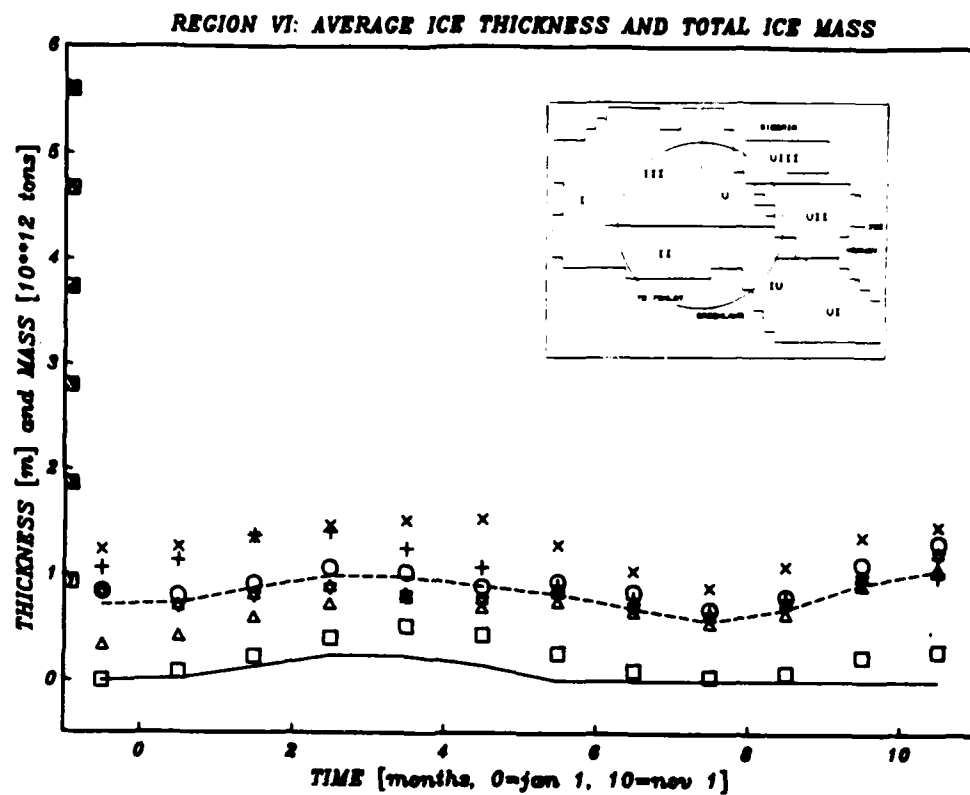


Figure A6 : As in Fig. A0 except for Region VI (Norwegian Sea).

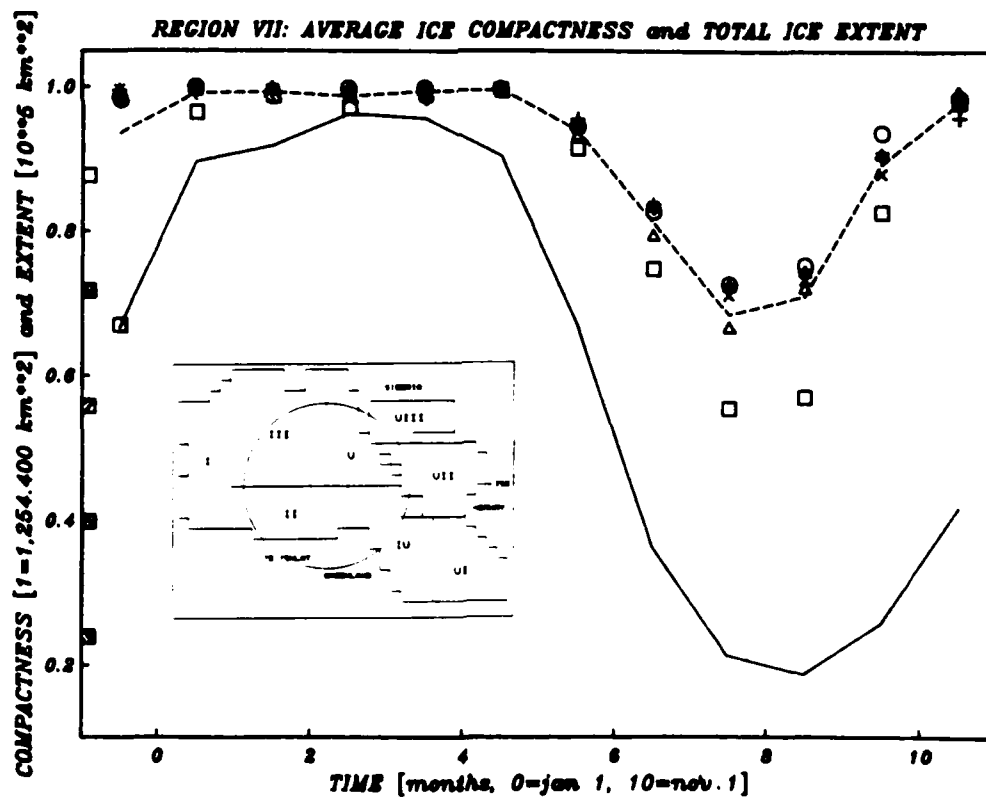
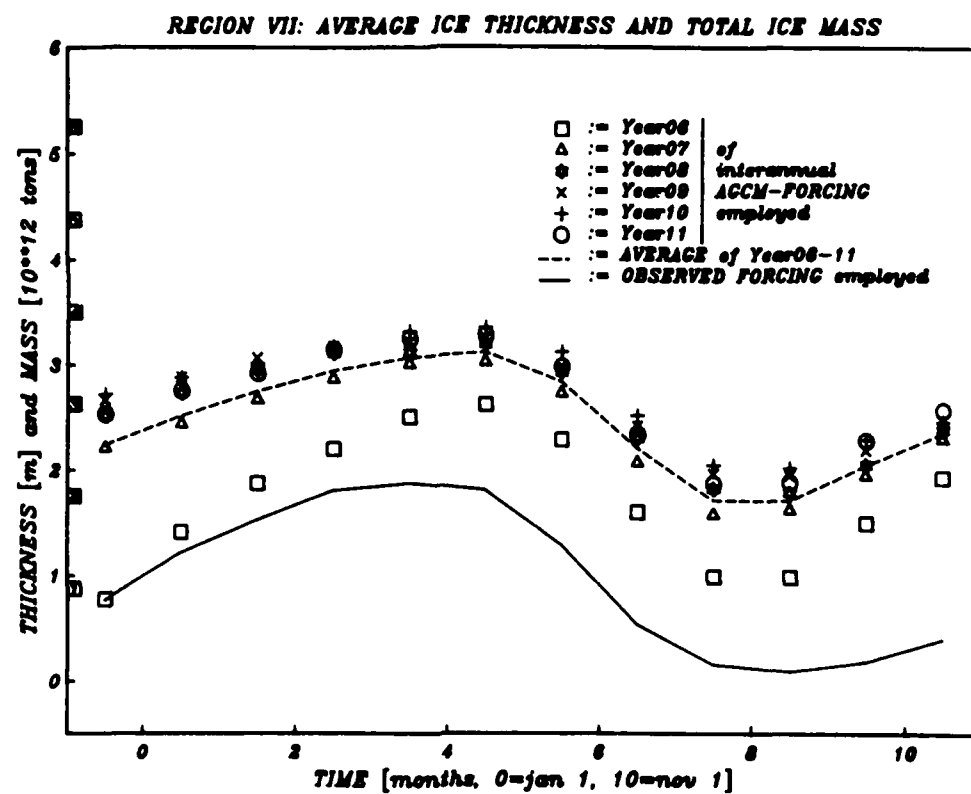


Figure A7: As in Fig. A0 except for Region VII (Barents Sea).

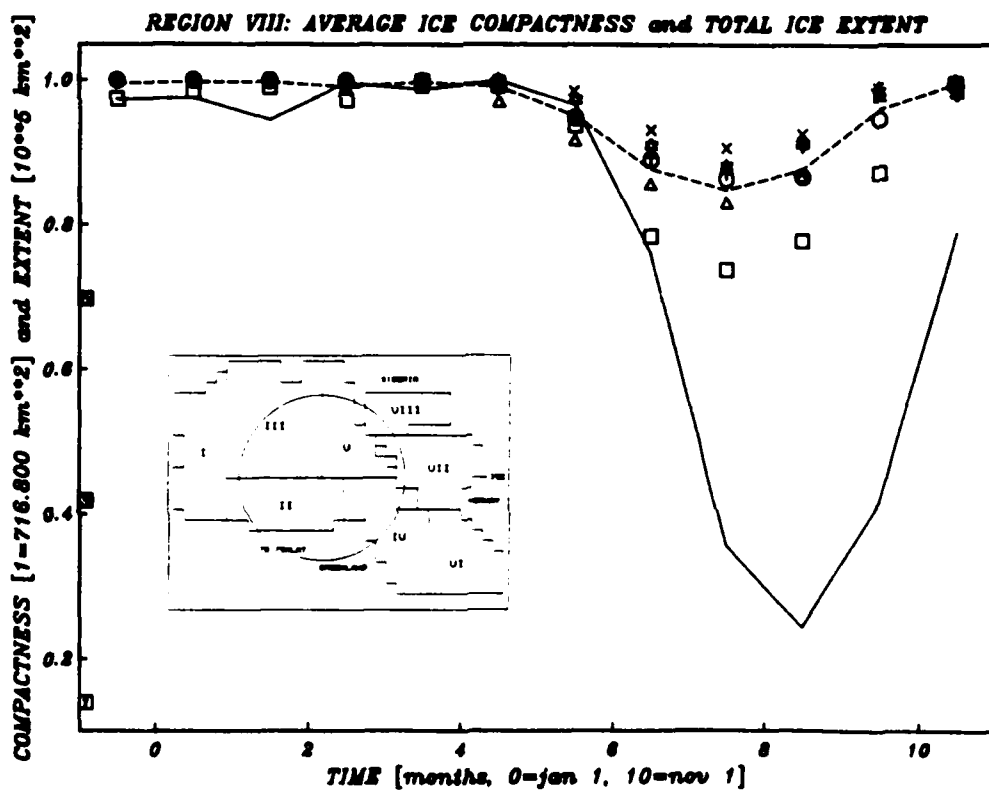
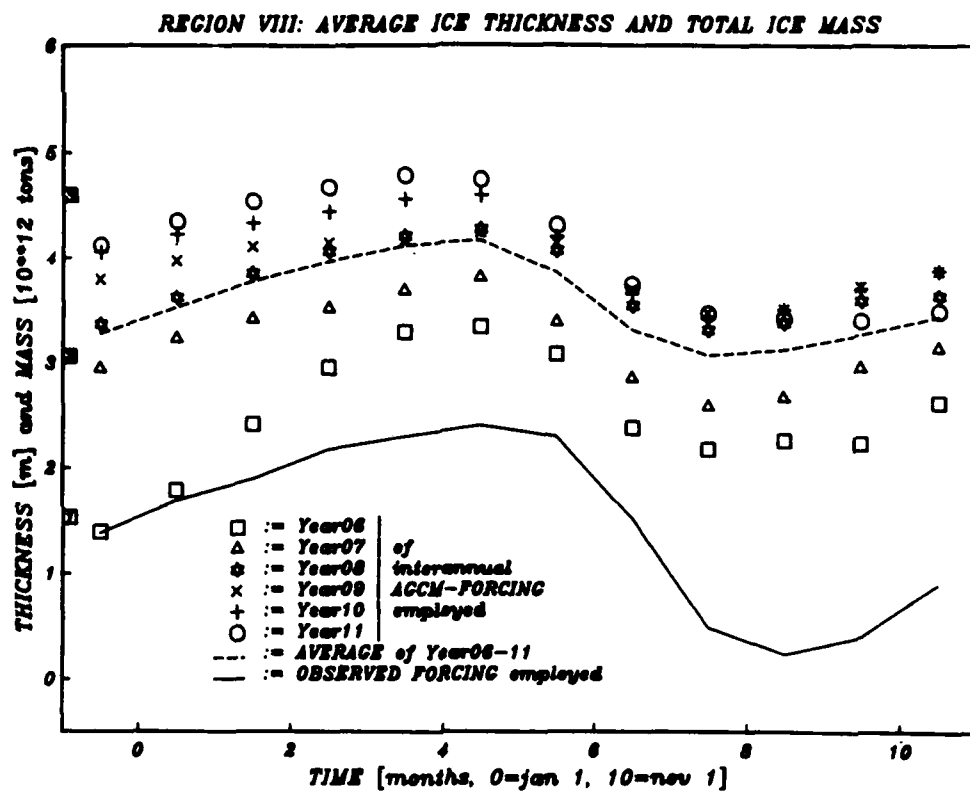


Figure A8 : As in Fig. A0 except for Region VIII (Kara Sea).

END

9-87

DTIC